Turbulence-distortion modelling for Amiet's theory enhancement

Piccolo, Andrea; Zamponi, Riccardo; Avallone, Francesco; Ragni, Daniele

DOI
10.1016/j.jsv.2025.119503

Publication date
2026

Document Version
Final published version

Published in
Journal of Sound and Vibration

Journal of Sound and Vibration 624 (2026) 119503

Contents lists available at ScienceDirect

Journal of Sound and Vibration

journal homepage: www.elsevier.com/locate/jsvi

Turbulence-distortion modelling for Amiet's theory enhancement

Andrea Piccolo [a,*], Riccardo Zamponi [a,b], Francesco Avallone [c], Daniele Ragni [a]

[a] Delft University of Technology, Kluyverweg 1, Delft, 2629 HS, The Netherlands
[b] von Kármán Institute for Fluid Dynamics, Waterloosest. 72, Sint-Genesius-Rode, 1640, Belgium
[c] Politecnico di Torino, Corso Duca degli Abruzzi 24, Torino, 10129, Italy

ARTICLE INFO

Keywords:
Leading-edge noise
Turbulence distortion
Analytical modelling

ABSTRACT

When applied to aerofoils with non-negligible thickness, Amiet's theory for turbulence-interaction noise prediction does not account for the alterations in the velocity field and acoustic response induced by the surface, resulting in an overestimation of the radiated noise. This study proposes a semi-analytical method that models turbulence distortion in the immediate vicinity of the surface starting from upstream flow conditions and considers the resulting effects on the acoustic response of the aerofoil. The distorted spectrum of the upwash velocity component is calculated using the asymptotic results of the rapid distortion theory (RDT) for very large- and small-scale turbulence, overcoming the need to define a representative location where turbulence characteristics are sampled. This distorted spectrum is characterised by an increased energy content that is encompassed in the model by scaling the analytical flat-plate formulation of the aeroacoustic transfer function. The proposed approach relies on defining the aerofoil geometrical feature that affects distortion mechanisms, required to extend the RDT results to such geometries. This parameter is identified as the path travelled by the turbulent eddies from the stagnation point to the position of maximum surface-pressure fluctuations, which is, in turn, related to flow acceleration and leading-edge sharpness. The accuracy of this methodology in enhancing noise prediction is demonstrated using numerical and experimental data of grid-generated turbulence interacting with different aerofoils.

1. Introduction

Low-fidelity noise-prediction models play a crucial role in the design and optimisation of wings and blades due to their lower computational cost compared to numerical simulations. In this case, far-field acoustic pressure is derived from a statistical characterisation of the flow field using analytical or semi-empirical relations to model sound-production mechanisms [1].

In the case of turbulence-interaction noise (also known and referred here as leading-edge noise), resulting from the impingement of turbulent structures on the leading edge of an aerofoil, the model formulated by Amiet [2] computes the power spectral density (PSD) of the far-field acoustic pressure using the velocity spectrum of the incoming turbulence and an aeroacoustic transfer function that models the acoustic response of the aerofoil to the incoming perturbation. The theory is developed under the assumptions of frozen turbulence and linearised aerofoil, meaning that the effects on turbulence and sound radiation of geometrical features, such as thickness, camber, and leading-edge radius, are neglected. As a result, Amiet's theory becomes less accurate in the high-frequency range in the case of aerofoils with non-negligible thickness, as observed by Paterson and Amiet [3], Moriarty et al. [4], and Moreau and Roger [5]. Therefore, despite the widespread use of the model, research to enhance its accuracy for more realistic geometries is ongoing [4–6].

* Corresponding author.
E-mail address: a.piccolo@tudelft.nl (A. Piccolo).

https://doi.org/10.1016/j.jsv.2025.119503
Received 13 August 2024; Received in revised form 15 October 2025; Accepted 16 October 2025
Available online 30 October 2025

Extensive research has been dedicated to identifying the aerofoil geometrical features affecting leading-edge noise. The deflection of the flow streamlines due to the aerofoil thickness was shown to reduce fluctuating lift and, consequently, sound production in the high-frequency range [7,8]. Sound attenuation was later found to be limited to downstream listener positions, while increased radiation was observed in the upstream direction [9–11]. Conversely, Oerlemans [12] and Hall et al. [13] noticed that the shape of the leading edge, rather than solely the aerofoil thickness, influences noise generation, with blunter aerofoils being less efficient at radiating sound. Chaitanya et al. [14] confirmed this conclusion, showing that aerofoil thickness influences noise at low frequencies, while the leading-edge radius has a more pronounced effect at high frequencies. This is aligned with the findings of Gill et al. [11], who attributed these effects to the distortion of the vortical gusts in the stagnation region caused by the velocity gradients near the leading edge. Turbulence-interaction noise was thus shown to be induced by the flow field in the stagnation region, as concluded by Bowen et al. [15] through the analysis of the coherence between surface-pressure and velocity fluctuations.

Leading-edge noise generation investigations have been accompanied by studies aimed at improving the accuracy of the noise prediction provided by low-fidelity methods. Moriarty et al. [4] achieved a good agreement with experimental data by implementing the analytical correction to Amiet's model proposed by Guidati et al. [16], which, however, relied on an empirical tuning constant of 10 dB. Interestingly, several methods introduced an exponential correction to model high-frequency thickness effects. This is the case of the work of Gershfeld [17], which showed a good match with the experimental results of Paterson and Amiet [3], and the ones of Lysak et al. [18] and Kim et al. [19]. In these latter cases, exponential corrections were derived by fitting data obtained for thick aerofoils and shown to depend on the Mach number, aerofoil thickness, and leading-edge radius.

The line of research introduced by Moreau and Roger [5] is particularly relevant to the present investigation. It involved correcting Amiet's model by accounting for the deformation of incoming turbulence occurring for thick aerofoil geometries, using the asymptotic results of the rapid distortion theory from Hunt [20,21]. These are closed-form analytical expressions obtained in Hunt's framework – describing the alteration of homogeneous isotropic turbulence interacting with a cylinder – for very large and very small scale turbulence with respect to the body. This is quantified in terms of the ratio between the integral length scale L_1 of the incoming turbulence and the body characteristic dimension a (equal to the cylinder radius), which also determines the prevailing distortion mechanism. For $L_1/a \gg 1$, i.e. very large structures interacting with the body, the blockage caused by the body prevails, inducing a momentum transfer from the streamwise to the upwash velocity component fluctuations. This can be observed looking at the root-mean-square and the wavenumber spectra of the two velocity components. For small-scale eddies ($L_1/a \ll 1$ or when the spatial wavenumber $k_1 \to \infty$), the distortion of the vorticity field dominates. The stretching and shortening of the vortex lines at the stagnation point cause an increase in the streamwise velocity fluctuations and a decrease in the upwash velocity ones, leading to a steeper decay slope of the spectrum of the latter at high wavenumbers.

The variation of the high-frequency decay of the upwash velocity component spectrum was used by Moreau and Roger [5] to modify the von Kármán spectrum, which serves as an input in Amiet's model to describe incoming turbulence. This approach, even though limited to the investigated case and relying on two case-specific constants, made it possible to improve the agreement with the experimental data obtained for a NACA 0012 and confirmed the potential benefit in terms of noise-prediction accuracy achievable by accounting for turbulence distortion. Similar approaches were proposed by Christophe [22], De Santana et al. [6], and dos Santos et al. [23,24]. They attempted to generalise the methodology of Moreau and Roger [5] imposing the conservation of the variance with respect to the upstream undistorted flow conditions. However, this approach neglects the alteration of the spectrum in the low-wavenumber range and the increase of the root-mean-square of the velocity fluctuations, which indicates a variation of the gust energy as it approaches the leading edge. This limitation, together with the reliance on the identification of a position in the stagnation region where turbulence characteristics should be sampled to scale the turbulence spectrum, limits the generality of the correction, as pointed out by the same authors. Piccolo et al. [25–27] sampled the turbulence spectrum, to be fed into Amiet's model, in the stagnation region of an aerofoil interacting both with large-scale rod-generated and grid-generated turbulence. This retrieved a better estimation of the high-frequency decay but also an overestimation of the noise levels, thus demonstrating a shortcoming in the modelling. The application of the RDT to aerofoils relies on the identification of an equivalent characteristic dimension a, which has yet to be conclusively identified. Mish and Devenport [28,29] proposed the leading-edge radius, while dos Santos et al. [30] argued that the average aerofoil thickness before the position of maximum thickness is the appropriate dimension to consider.

A wide body of research has been dedicated to investigating the effects of aerofoil geometry on the acoustic response, modelled by the aeroacoustic transfer function. Indeed, while an analytical expression can be derived for a flat plate, more advanced analytical or numerical approaches are required to account for the effects of finite thickness on the loading distribution, as demonstrated in the works of De Santana [31] and Miotto et al. [32]. A significant enhancement to the description of realistic geometries response has been brought by the works of Christophe [22] and De Santana [31], who applied the trailing-edge noise methodology of Roger and Moreau [33] and Moreau and Roger [34] to include a back-scattering correction to Amiet's original formulation for leading-edge noise.

In view of the above, a clear yet scattered framework emerges for the enhancement of leading-edge noise low-fidelity predictions in the case of realistic aerofoil geometries. Regarding the description of the altered turbulent field interacting with the aerofoil, the RDT has played a seminal role, though several shortcomings limit the general validity of currently implemented methodologies. Conversely, procedures developed to improve the modelling of the acoustic response via the aeroacoustic transfer function still depend on cumbersome numerical methods. What emerges is the need for an organic and general corrective approach to account for the aerofoil-geometry effects in leading-edge noise prediction, which has yet to be defined.

The present study proposes a turbulence-distortion modelling methodology to enhance Amiet's model by predicting the alteration of the velocity field at the stagnation point and accounting for the resulting effects on the aerofoil acoustic response. This approach is based on the use of the asymptotic results of the RDT to calculate the alteration of the upwash velocity component spectrum

and the variation of the upwash-gust energy starting from upstream flow conditions. The application of RDT results for aerofoil configurations has been made possible through the identification of the geometrical feature affecting turbulence distortion for such geometries. The result is the formulation of a consistent and systematic procedure to enhance the noise prediction using only upstream undistorted flow characteristics (integral length scale and turbulence intensity) and the characteristic "distortion length", eliminating the need to specify a position in the stagnation region for sampling distorted-turbulence characteristics.

This methodology is supported by the findings of the physical investigation conducted by Piccolo et al. [26], which are here extended to additional aerofoil geometries and loading conditions. Building on these results, the present analytical study entails three conceptual steps: (i) generalising the physical insights from Piccolo et al. [26]; (ii) formulating analytical expressions to model the observed behaviour and characterise turbulence interaction with aerofoil geometries; and (iii) incorporating these expressions into a general framework, i.e. the proposed turbulence-distortion modelling methodology.

This work has been indeed validated through four numerical simulations of three aerofoils, NACA 0012, NACA 0012-103 (analysed also in Piccolo et al. [26]), and NACA 4412, interacting with grid-generated turbulence under zero lift and loading conditions. The simulations, conducted using the Lattice-Boltzmann method-based software PowerFLOW, replicate the experimental set-up of Chaitanya et al. [14], who investigated leading-edge noise for various aerofoil geometries.

The paper is organised as follows. Section 2 reports information on the flow solver and the numerical set-up. The distortion length for aerofoil configurations is introduced in Section 3, while the proposed methodology to correct Amiet's model by including distortion effects is detailed in Section 4. The application of the methodology is reported in Section 5, with the conclusions drawn in Section 6.

2. Methodology

2.1. Flow solver

The numerical investigation has been carried out using the commercial software Simulia PowerFLOW 6-2021, which employs the Lattice-Boltzmann method (LBM) to compute the flow field. This technique uses a statistical gas kinetic model to compute the advection and collision of fluid particles along a finite number of predefined directions. These are modelled by particle-distribution functions, whose local integration yields flow quantities, such as density, momentum, and internal energy [35]. The implemented discretisation of the Boltzmann equation, performed on a Cartesian mesh (lattice), employs 19 discrete velocity vectors in three dimensions, i.e. D3Q19, with a third-order truncation of the Chapman-Enskog expansion. In the assumptions of perfect gas at low Mach numbers and isothermal conditions, this approach was proven to be accurate for the approximation of the Navier–Stokes equation [36]. The collision operator is based on the Bhatnagar–Gross–Krook (BGK) model [37], formulated as a function of the relaxation time, which depends on fluid viscosity, temperature, and the Maxwell–Boltzmann equilibrium distribution function F_i^{eq} [36]. The implemented approach builds on the work of Chen et al. [38], Chen et al. [39], allowing the solver to be extended to high-speed flows and low-viscosity regimes [40,41].

Sub-grid unresolved scales of turbulence are handled by the solver using a very-large-eddy simulation (VLES) approach. A modified two-equation $k-\epsilon$ re-normalisation group formulation is used to calculate an effective relaxation time τ_{eff}, obtained by adding a turbulent relaxation time to the viscous one [42]. This modification also prevents numerical damping of large-scale structures by reducing the subgrid-scale viscosity [43]. The modified relaxation time τ_{eff} is then used to adapt the Boltzmann model to the characteristic time scales of the turbulence in the flow, allowing the development of large-scale eddies. Therefore, in the LBM-VLES approach, the turbulence model is used to modify and continuously update the relaxation properties of the system. The Reynolds stress results from the chaotic exchange of momentum inherently related to the turbulent motion, and their non-linearity is indeed correctly modelled thanks to the Chapman-Enskog expansion. As a result, the model is well suited to represent turbulence in a state far from equilibrium, as in the presence of distortion and shear [44].

The unit element of the three-dimensional mesh grid in which the domain is discretised is referred to as voxel, while surfels (i.e. surface elements) are generated by the intersection of voxels with solid boundaries. The solver applies a wall function in the first domain unit cell close to the surface, allowing the no-slip boundary condition to be approximated. This function is based on an extension of the generalised law-of-the-wall model, accounting for the effects of pressure gradients [45].

The discretisation of the whole numerical domain is carried out by using refinement regions of increasing resolution towards the zones of interest, with the size of the voxel varying by a factor of 2 across adjacent regions. High resolution is maintained only in aerodynamically significant regions and acoustic analogies are employed to compute far-field acoustic pressure.

The formulation 1 A of Farassat and Succi [46] of the Ffowcs-Williams and Hawkings (FWH) acoustic analogy with forward-time solution [47] has been used to calculate far-field noise. This has been obtained using pressure fluctuations sampled on the aerofoil surface, with the purpose of considering only the acoustic dipoles and monopoles [48] and neglecting quadrupole sources.

2.2. Computational domain

The numerical set-up, shown in Fig. 1, reproduces the open-jet wind-tunnel facility at the Institute of Sound and Vibration Research (ISVR) at the University of Southampton, where the experimental campaign of Chaitanya et al. [14] has been carried out. The same numerical set-up has been used and validated also in Piccolo et al. [26]. The simulation domain, whose size does not correspond to the actual dimensions of the anechoic chamber for computational requirements, consists of a cube of 5 m side centred at the aerofoil leading edge (in the cases where the angle of attack is equal to zero). This coincides with the origin of the reference

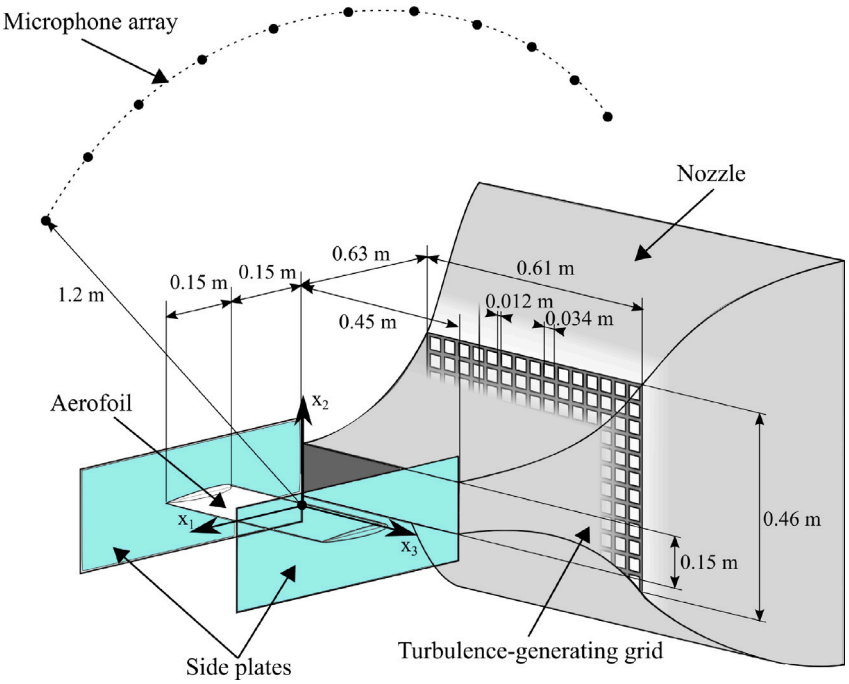

Fig. 1. Drawing of the numerical set-up (not to scale). The most relevant dimensions and separation distances are reported together with the geometrical features of the turbulence-generating grid.

frame, whose axes are denoted as x_1, x_2, and x_3, representing the streamwise, upwash, and spanwise directions, respectively. The corresponding velocity components are u_1, u_2, and u_3, while the spatial wavenumbers are indicated with k_1, k_2, and k_3. The chord of the aerofoil is $c = 0.15\,\mathrm{m}$, while its span is $L = 0.45\,\mathrm{m}$. It is placed 1 chord downstream of a convergent nozzle having a rectangular exit section 0.45 m wide and 0.15 m high and a square inlet section of side 1.3 m. The converging part of the ISVR nozzle is 1.35 m long, but in the numerical set-up the tunnel has been extended upstream with a constant square-section duct to allow the inlet boundary conditions to be applied directly at the boundary of the simulation domain. At the exit section of the nozzle, on the sides of the aerofoil, two rectangular plates 0.225 m high and 0.375 m long have been placed to eliminate tip effects. In both the experimental and numerical set-ups, turbulence is generated by a rectangular grid measuring $0.46\,\mathrm{m} \times 0.61\,\mathrm{m}$ and positioned 0.63 m upstream of the nozzle exit. The square rods of the turbulence-generating grid, separated by a distance equal to 0.034 m, have a thickness of 0.012 m, resulting in a solidity of 55 %.

The total pressure at the nozzle inlet has been imposed to achieve a free-stream velocity of $U_\infty = 60\,\mathrm{m\,s^{-1}}$ at $x_1/c = -0.033$ without the aerofoil in the open jet. This free-stream velocity corresponds to a Reynolds number, with respect to the aerofoil chord, of $Re = 6.2 \times 10^5$. The head loss caused by the presence of the turbulence-generating grid has been taken into account using the empirical results of Roach [49], while the friction loss along the nozzle walls has been neglected in the numerical simulation. On all the other boundaries of the cubic domain, a static pressure of 101 325 Pa has been imposed.

10 voxel-refinement regions have been used to discretise the numerical domain at the finest grid resolution. The turbulence-generating grid and the aerofoil are placed into the same refinement region to avoid any variation of the voxel size, which here is 7.19×10^{-4} m, and affect turbulence convection. The voxel size is further reduced along the aerofoil surface by means of two refinement regions obtained as offsets of the aerofoil geometry, reaching a value of 1.79×10^{-4} m along the aerofoil surface. This leads to an average value of y^+ along the surface of the body of 19. The finest resolution configuration hence requires a discretisation of the numerical domain into a total of 660×10^6 voxels.

The simulation time is 0.2295 s, corresponding to 92 flow-through times. After a transient of 25 flow-through times, i.e. 0.0625 s, flow quantities have been saved for 0.1670 s, equivalent to 10 repetitions of the cycle at the lowest frequency of interest (60 Hz) and to 67 flow-through times. The physical time step, depending on the grid resolution, is equal to 3.046×10^{-7} s for the finest configuration. The grid-independence study, together with the aerodynamic and acoustic validations of the numerical simulations, is reported in Appendix A (see also Piccolo et al. [26] for a more detailed discussion).

The solid formulation of the FWH analogy, using the pressure sampled on the aerofoil surface, has been employed to calculate the far-field acoustic radiation. A 30 kHz acquisition frequency has been imposed to obtain flow quantities on the aerofoil surface and in the flow field. The power spectral densities have been computed by means of Welch's method, using a Hanning window with 50 % overlap resulting in a frequency resolution of 100 Hz. The direct far-field noise has also been computed using probes placed along a circle arc in the midspan plane of the aerofoil (Fig. 1). This arc, centred at the origin of the numerical domain, features a

Table 1
Investigated configurations and geometrical information of the four analysed aerofoils.

NACA	Chord, c (m)	Span, L (m)	LE radius, r_{LE} (m)	Angle of attack, α (deg)
0012	0.15	0.45	2.4×10^{-3}	0
0012–103	0.15	0.45	6.6×10^{-3}	0
4412	0.15	0.45	2.4×10^{-3}	−3.89 1

radius $R = 1.2\,\mathrm{m}$ and ranges from $\theta = 2\pi/9$ and $\theta = 7\pi/9$, with the angle measured with respect to the downstream direction. The angular separation between the 11 probes is $\Delta\theta = \pi/18$.

Three different aerofoils have been investigated in the numerical simulations. The baseline aerofoil is a standard NACA 0012, compared to a NACA 0012-103 to evaluate the effect of leading-edge radius and to a NACA 4412 to examine the impact of aerofoil camber. All three aerofoils share the same thickness distribution. While the NACA 0012 and NACA 0012-103 are included in the experimental study by Chaitanya et al. [14], the NACA 4412 is not. The radius of the leading edge for the standard NACA 0012 and the NACA 4412 is 2.4×10^{-3} m, while it is equal to 6.6×10^{-3} m for the NACA 0012-103. All the aerofoils have been tested at zero loading conditions, which correspond to an angle of attack of $\alpha = 0°$ for the symmetric NACA 0012 and NACA 0012-103 and an angle of attack of $\alpha = -3.89°$ for the cambered NACA 4412. The latter has also been analysed at lifting conditions, selecting an angle of attack α equal to 1°. In the cases of the cambered aerofoil, positioned at incidence different from zero, the angle of attack has been obtained by rotating the aerofoil around the position at $\frac{1}{4}$ of the chord. All the information regarding the geometry of the aerofoils is reported in Table 1.

The curvature of the aerofoil has also been taken into account to analyse the effects of aerofoil geometry on the distortion of the incoming turbulent eddies. Indicating with x_{NACA} and y_{NACA} the coordinates of the NACA aerofoil geometries, the non-dimensional aerofoil curvature C_s has been obtained as

$$C_s = \left(\frac{1}{r_{LE}}\right) \frac{\ddot{y}_{NACA}}{\left(1 + \dot{y}_{NACA}^2\right)^{3/2}}.$$

The dot indicates the derivation of y_{NACA} with respect to x_{NACA}, while the non-dimensionalisation has been performed using the leading-edge radius.

3. Distortion mechanism for realistic aerofoil geometries

The application of the RDT for an aerofoil depends on the identification of the geometrical parameter a with respect to which the scale of the incoming turbulence L_1 shall be compared, for which no agreement in the literature has been reached yet. To this aim, the surface-pressure distribution on the aerofoil leading edge for the numerical configurations is investigated to gain knowledge on the geometry effects on turbulence distortion and noise generation. The analysis builds on the results of Piccolo et al. [26], obtained for symmetrical aerofoils, and extends them to the cambered and loaded geometries examined in this study. The non-dimensional pressure gradient along the surface and the root-mean-square of the surface-pressure fluctuations are shown in Fig. 2 for the numerical configurations considered. These two quantities have been plotted with respect to the curvilinear abscissa s, which originates at the trailing edge and is directed from the upper to the lower side of the aerofoil. The leading edge is localised around $s/c = 1$, depending on the camber and the aerofoil curvature, while the position of the stagnation point is determined by the flow incidence. In the case of the symmetrical aerofoils at a zero angle of attack, the leading edge and stagnation point coincide (Figs. 2(a) and 2(b)), resulting in $s_{stag} \simeq s_{LE}$. For the NACA 4412 at zero-lift conditions, the stagnation point is on the upper side of the aerofoil, i.e. $s_{stag} < s_{LE}$ (Fig. 2(c)), while, at lifting conditions, it is placed on the lower side, i.e. $s_{stag} > s_{LE}$ (Fig. 2(d)).

For both symmetrical and cambered aerofoils, two peaks of the root-mean-square of the surface-pressure fluctuations are found in the vicinity of the stagnation point, on the pressure and the suction side. As expected, the two symmetrical aerofoils feature symmetric peaks on the two sides, whereas this is not the case for the cambered configurations. These peaks are further apart in the case of the NACA 0012-103, which features a larger leading-edge circle with respect to the baseline NACA 0012. Interestingly, in all four configurations, surface-pressure fluctuations and pressure gradient reach the maximum value almost at the same positions on the pressure and suction sides, with the latter peaking slightly closer to the stagnation point.

As proposed by Piccolo et al. [26], the results suggest that the increase in unsteady surface pressure, typically associated with sound generation, may be related to the flow acceleration due to the pressure gradients caused by the leading-edge curvature. Therefore, it can be assumed that the acceleration can be responsible for the deformation of the turbulent structures impinging on the aerofoil. As a consequence, considering a turbulent eddy convected along a streamline curved by the action of the aerofoil on the flow, the size of the eddy with respect to the space available to accelerate on the pressure and the suction sides of the aerofoil impacts its deformation during the interaction with the surface. This "distortion length" can be estimated by considering the length along the leading edge from the stagnation point to the two positions where the surface-pressure fluctuations peak on the pressure and suction sides of the aerofoil. A good estimate of this length can be thus obtained by halving the distance between these two

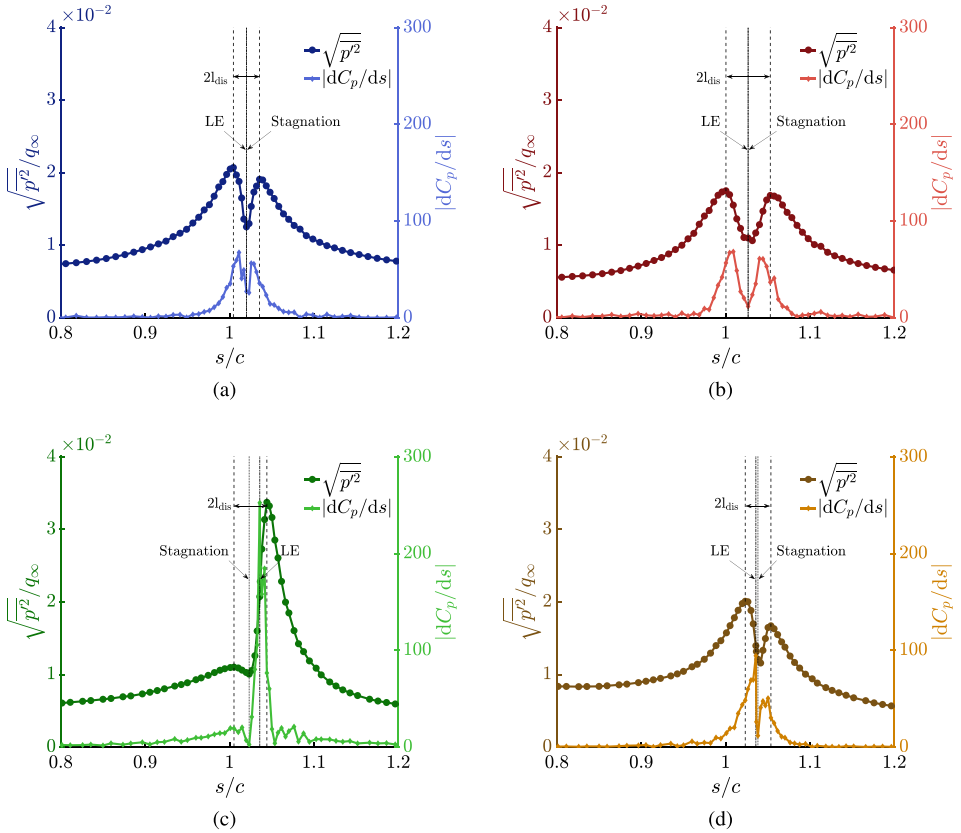

Fig. 2. Distribution of the time-averaged pressure gradient and root-mean-square of the surface-pressure fluctuations with respect to the curvilinear abscissa s for the (a) NACA 0012, (b) NACA 0012-103, (c) NACA 4412 at $\alpha = \alpha_{ZL}$, and (d) NACA 4412 at $\alpha = 1°$.

Table 2
"Distortion length" for the 4 aerofoil configurations. The ratio L_1/a is reported as well. The RDT parameter a has been taken equal to l_{dis}, estimated by halving the distance between the positions where the root-mean-square of the surface pressure fluctuations peaks on the two sides of the aerofoil.

NACA	$l_{dis} = a$ (m)	L_1/a (−)
0012	2.40×10^{-3}	2.50
0012–103	3.30×10^{-3}	1.80
4412, $\alpha = \alpha_{zl}$	2.90×10^{-3}	2.00
4412, $\alpha = 1°$	2.20×10^{-3}	2.66

positions. This parameter, denoted as l_{dis}, is chosen as the geometrical characteristic dimension a to be used for the application of the RDT in the case of more realistic aerodynamic surfaces. The corresponding values for the 4 numerical configurations considered are reported in Table 2.

It is worth now investigating the potential links between the surface-pressure distribution and the aerofoil geometry to identify a practical criterion to determine l_{dis} and hence the parameter a without the knowledge of the flow field. Fig. 3 shows the time-averaged surface pressure gradient along s together with the derivative of the aerofoil-surface curvature. In the case of the symmetrical aerofoils at a zero angle of attack, a correspondence exists between the position where the root-mean-square of the pressure fluctuations reaches its maximum value, the location where pressure gradient peaks, and the curvilinear abscissa where the curvature of the aerofoil changes more abruptly. For both NACA 0012 and NACA 0012-103, the pressure gradient and curvature derivative peaks occur slightly earlier than the maximum surface pressure fluctuations. While a similar physical behaviour is observed for the cambered aerofoil, with the surface-pressure fluctuations peaking alongside the pressure gradient because of the

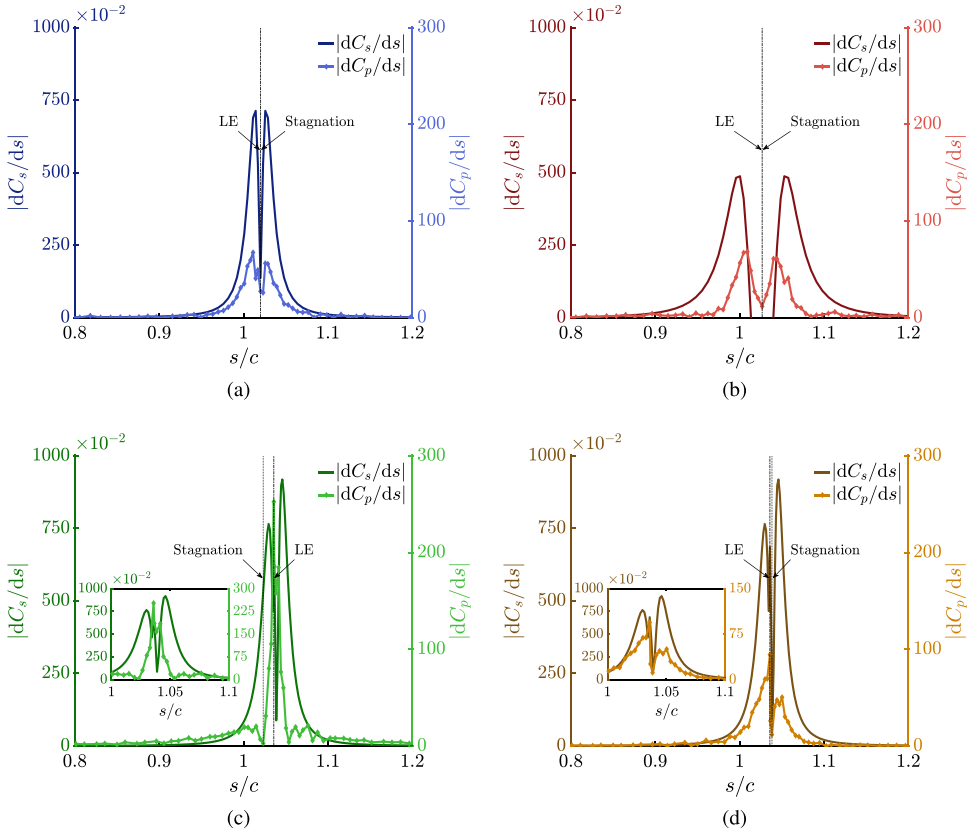

Fig. 3. Distribution of the aerofoil surface-curvature derivative and the time-averaged pressure gradient with respect to the curvilinear abscissa s for the (a) NACA 0012, (b) NACA 0012-103, (c) NACA 4412 at $\alpha = \alpha_{ZL}$, and (d) NACA 4412 at $\alpha = 1°$.

strong curvature variation, there is no exact correspondence between these peak positions, neither at zero loading condition (Fig. 3(c)) nor at a small incidence (Fig. 3(d)).

These observations thus identify a relationship between the pressure gradient, which induces the flow acceleration and the deformation of the turbulent structures, with the curvature of the flow around the leading edge. In the case of symmetrical thin aerofoils at zero angle of attack, the flow follows the aerofoil surface, explaining the correspondence between the peaking positions of the curvature derivative and the pressure gradient. Therefore, a possible way to estimate a knowing only the aerofoil geometry is by evaluating $|\mathrm{d}\,C_s/\mathrm{d}\,s|$, for instance using the panel method code XFOIL [50]. This will be evaluated in Section 5.2 using XFOIL data to validate the proposed methodology against the experimental data of Chaitanya et al. [14]. Regarding the cambered aerofoils, while the physical description of the distortion mechanism remains valid, further investigations are needed to establish an equivalent procedure for estimating the reference geometric parameter for RDT applications solely from geometrical and aerodynamic data known *a priori*.

4. Turbulence-distortion modelling for low-fidelity noise-prediction methods

The proposed methodology aims to calculate, starting from undistorted turbulence data at upstream conditions, the alteration of the velocity field and acoustic response induced by turbulence distortion. Referring to Amiet's formulation for large-span aerofoils (Eq. (B.6)), this is achieved by modelling the alteration of the turbulence frequency spectrum Θ_{22} and the spanwise coherence length $l_3(\omega)$ of the upwash velocity component, and the aeroacoustic transfer function $\mathcal{L}$.

The corrections, detailed in Sections 4.1–4.3, result in the following formulation for a distortion-corrected Amiet's model to retrieve the PSD of the far-field acoustic pressure $S_{pp}(\omega)$ at a listener position $\mathbf{x} = (x_1, x_2, 0)$:

$$S_{pp}(x_1, x_2, 0, \omega) = \left(\frac{\omega x_2 \rho_\infty c M_\infty}{2\sigma^2}\right)^2 \frac{L}{2} \left|\mathcal{L}_{\mathrm{dis}}(\mathbf{x}, K_1, 0)\right|^2 \Theta_{22,\mathrm{dis}}(\omega)\, l_{3,\mathrm{mod}}(\omega). \tag{1}$$

Here, $\sigma = \sqrt{x_1^2 + \beta^2(x_2^2 + x_3^2)}$, with $\beta = \sqrt{1 - M_\infty^2}$, accounts for the effects of convection, $M_\infty = U_\infty/c_\infty$ is the free-stream Mach number, with c_∞ indicating the speed of sound, $K_1 = \omega/U_\infty$ is the streamwise wavenumber in the assumption of frozen turbulence, and ρ_∞ is the flow density. For a detailed derivation of the expression, the reader is referred to Appendix B, where Amiet's theory for leading-edge noise is presented.

4.1. Distorted-turbulence spectrum modelling

In the asymptotic cases of very large-scale and very small-scale turbulence, the four partial differential equations derived by Hunt [20] in the RDT framework to model the distorted field from upstream conditions are simplified into closed-form analytical expressions.

The semi-analytical method discussed here entails the interpolation of these equations to retrieve a single expression for $\Theta_{22,\mathrm{dis}}$ valid on the whole wavenumber range. This holds true under the assumption $L_1/a > 1$, which justifies the use of the asymptotic result obtained for large-scale turbulence to model the alteration of the spectrum in the low-wavenumber range ($k \to 0$). This procedure allows the distorted spectrum near the stagnation point to be estimated using only the intensity and integral length scale of the upstream undistorted turbulence as inputs, along with the geometrical characteristic length of the aerofoil.

4.1.1. Asymptotic analyses in the case of large-scale turbulence and low-wavenumber alteration modelling

For large-scale turbulence ($L_1/a \gg 1$), the asymptotic analysis of Hunt [20] leads to the following expression for the one-dimensional distorted spectrum of the upwash velocity component $\Theta_{22,\mathrm{dis}}$ along the stagnation streamline:

$$\Theta^*_{22,\mathrm{dis}}\left(\kappa_1\right) = \underbrace{\left[1 + \frac{1}{\left(1 - \frac{x_1}{a}\right)^2}\right]^2}_{\lambda_2^2(x_1)} \Theta^*_{22,\mathrm{ups}}\left(\kappa_1\right). \tag{2}$$

The derivation of this expression, which does not explicitly appear in Hunt [20], is provided in Appendix C. The superscript * indicates non-dimensional variables, with the one-dimensional spectrum $\Theta^*_{ij}\left(\kappa_i\right)$ obtained as

$$\Theta^*_{ij}\left(\kappa_i\right) = \frac{L_1}{a}\frac{\Theta_{ij}\left(k_i\right)}{u_i'^2 L_1}, \tag{3}$$

$\boldsymbol{\kappa}$ being the non-dimensional wavenumber calculated as

$$\boldsymbol{\kappa} = \begin{pmatrix} \kappa_1 \\ \kappa_2 \\ \kappa_3 \end{pmatrix} = a \begin{pmatrix} k_1 \\ k_2 \\ k_3 \end{pmatrix}.$$

Eq. (2) indicates that the alteration of the velocity spectra consists of an increase in the upwash velocity component with respect to the upstream undistorted conditions. A factor $\lambda_2^2\left(x_1\right)$, depending on the distance from the stagnation point, is employed to represent this variation, which is related to the momentum transfer from the streamwise to the upwash velocity component occurring for large-scale turbulence, as explained by Hunt [20] and in Section 1.

The alteration of the velocity spectra in the low-wavenumber range for an aerofoil can thus be evaluated by extending the analytical relations derived for the cylinder case. By replacing x_1 with a curvilinear abscissa ξ_1 for the distance along a generically curved stagnation streamline, it is finally obtained

$$\Theta_{22,\mathrm{dis}}\left(k_1\right)\Big|_{\mathrm{lowk}} = \lambda_2^2\left(\xi_1\right)\Big|_{\xi_1=0} \Theta_{22,\mathrm{vK}}\left(k_1\right), \tag{4}$$

with $\Theta_{22,\mathrm{vK}}$ indicating a canonical von Kármán expression (see Eq. (A.4)) employed to model the upstream undistorted flow conditions. The alteration in the immediate vicinity of the stagnation point can be described by considering the distance from the stagnation point $\xi_1 \to 0$, which results in $\lambda_2^2(0) \approx 4$.

4.1.2. Asymptotic analyses in the case of small-scale turbulence and high-wavenumber alteration modelling

In the high-wavenumber range, Hunt [20] showed that the spectrum of the upwash velocity component in the immediate vicinity of the stagnation point decays with an exponential slope according to

$$\Theta^*_{22,\mathrm{dis}}\left(\kappa_1\right) \simeq G_1 \left(a/L_1\right)^{-\frac{2}{3}} \kappa_1^{-\frac{7}{3}} \mathrm{e}^{-\frac{1}{2}\pi\kappa_1}, \tag{5}$$

where $G_1 = 0.0566$. Note that Eq. (6) is non-dimensional and will be converted to dimensional form by multiplying it by $u_1'^2 L_1$ and by a/L_1 (see Eq. (3)). Additionally, it is important to highlight that this expression is obtained from Eq. (C.1), which calculates the spectrum by performing two integrations between $-\infty$ and ∞ of a double-sided spectrum. Consequently, a factor 8 is necessary for comparison with one-dimensional single-sided spectra.

In the high-wavenumber range, the alteration of the upwash velocity spectrum in the case of an aerofoil can hence be modelled through

$$\Theta_{22,\mathrm{dis}}\left(k_1\right)\Big|_{\mathrm{highk}} = 8\left(u_1'^2 L_1\right)\left(a/L_1\right) G_1 \left(a/L_1\right)^{-\frac{2}{3}} \left(ak_1\right)^{-\frac{7}{3}} \mathrm{e}^{-\frac{1}{2}\pi a k_1}. \tag{6}$$

The small-scale turbulence limit formally holds for $k_1 \to \infty$. However, considering that this expression models the attenuation of the upwash velocity fluctuation with respect to upstream undistorted conditions, the proposed semi-analytical method adopts Eq. (6) for $k_1 > k_{1,\mathrm{CP}}$, with $k_{1,\mathrm{CP}}$ indicating the intersection with the von Kármán spectrum describing undistorted turbulence (the subscript CP standing for "crossing point").

Table 3
Cartesian coordinates of the sampling positions of the turbulence characteristics in the undistorted ($\xi_{1,\mathrm{ups}}$) and distorted ($\xi_{2,\mathrm{ups}}$) flow-field regions selected to assess turbulence-distortion effects.

NACA	$\xi_{1,\mathrm{ups}}$		$\xi_{1,\mathrm{dis}}$	
	$x_{1,\mathrm{ups}}$ (m)	$x_{2,\mathrm{ups}}$ (m)	$x_{1,\mathrm{dis}}$ (m)	$x_{2,\mathrm{dis}}$ (m)
0012	−0.075	0	1.50×10^{-5}	0
0012–103			1.50×10^{-5}	0
4412, $\alpha=\alpha_{zl}$			1.61×10^{-5}	-1.56×10^{-3}
4412, $\alpha=1°$			3.32×10^{-4}	4.76×10^{-3}

4.1.3. Mid-wavenumbers interpolation

Differently from the very large and very small-scale turbulence limit cases, the transition region before $k_{1,\mathrm{CP}}$ lacks any empirical or theoretical description providing simplified analytical relations and can be derived only through the solution of the RDT equations [20].

In order to finalise the semi-analytical method and provide a continuous piece-wise spectrum as an output, the distorted spectrum in this wavenumber range has been modelled by merging the analytical equations of the two limit cases. The expression used for low wavenumbers is considered valid up to $k_1 = k_{1,\mathrm{CP}}$ but it is multiplied by an exponential function, which models the decay in the high-wavenumber range, to obtain a continuous and gradual transition. The alteration of the upwash velocity spectrum in the low and the mid-wavenumber region will be thus described by

$$\Theta_{22,\mathrm{dis}}\left(k_1\right)\Big|_{\mathrm{low-midk}} = \Theta_{22,\mathrm{dis}}\left(k_1\right)\Big|_{\mathrm{lowk}} \mathrm{e}^{Bk_1} = \lambda_2^2\left(\xi_1\right)\Big|_{\xi_1=0}\Theta_{22,\mathrm{vK}}\left(k_1\right)\mathrm{e}^{Bk_1}, \tag{7}$$

with the coefficient B determined by imposing the continuity of the function at $k_1 = k_{1,\mathrm{CP}}$.

Finally, the distortion-corrected upwash velocity spectrum yielded by the proposed semi-analytical method will hence read

$$\Theta_{22,\mathrm{dis}}\left(k_1\right) = \begin{cases} \lambda_2^2\left(\xi_1\right)\Big|_{\xi_1=0}\Theta_{22,\mathrm{vK}}\left(k_1\right)\mathrm{e}^{Bk_1}, & k_1 \le k_{1,\mathrm{CP}} \\ 8\left(u_1'^2 L_1\right) G_1\left(a/L_1\right)^{\frac{1}{3}}\left(a\,k_1\right)^{-\frac{7}{3}}\mathrm{e}^{-\frac{1}{2}\pi a k_1}, & k_1 \ge k_{1,\mathrm{CP}} \\ . \end{cases} \tag{8}$$

The expression for $\Theta_{22,\mathrm{dis}}$ is of differentiability class C^0, since the derivative is not continuous at $k_{1,\mathrm{CP}}$.

Fig. 4 shows the validation of the upwash velocity spectra provided by Eq. (8) and the numerical ones obtained with PowerFLOW (PF in the plots) in the stagnation region. These spectra are displayed as a function of the Strouhal number, St_{t}, calculated using the aerofoil thickness, to be consistent with the investigation of Chaitanya et al. [14]. Being ξ_1 the distance from the stagnation point along the stagnation streamline, the numerical upwash velocity spectra have been considered far upstream from the leading edge ($\xi_{1,\mathrm{ups}}/c = -0.5$) and in the immediate vicinity of the stagnation point ($\xi_{1,\mathrm{ups}}/c = -1.5\times10^{-3}$). The coordinates of these positions are reported in Table 3, while the L_1/a ratios for the four configurations are reported in Table 2 (information about the integral length scale is reported in Appendix A). Such position is not required to retrieve the semi-analytical spectra, calculated in the limit $\xi_1 \to 0$.

With the exception of the mid-frequencies range, the semi-analytical method proposed herein is able to provide a good estimate of the alteration of the upwash velocity component spectrum using as input only the upstream undisturbed values of the turbulence integral length scale and intensity. The slight discrepancy observed in the low-frequency range is due to the small flow anisotropy caused by the strong contraction of the nozzle (see Appendix A and Piccolo et al. [26]). This is not taken into account in the present application of the model, which employs a von Kármán expression, valid in the case of homogeneous isotropic turbulence, to describe upstream flow characteristics. As a matter of fact, slight anisotropic turbulence conditions in the upstream flow could be accounted for using *ad hoc* analytical expressions for the velocity spectrum as input in the semi-analytical method.

These results prove that this approach represents a viable and efficient tool to model the alteration of the upwash velocity component spectrum caused by turbulence distortion.

The semi-analytical method is generalised beyond the narrow range of L_1/a considered by comparing the resulting distorted spectra with those provided by the solution of the RDT equations. This implementation, based on the work of Zamponi et al. [51] and validated against experimental data, allows the modelling of the alteration of the velocity field through Eq. (C.1) for any L_1/a ratio using as input only the analytical expression for a velocity spectrum describing homogeneous isotropic flow conditions. However, the high computational cost associated with the implementation of this formulation prevents it from being directly used to enhance the low-fidelity prediction.

The comparison between the distorted upwash velocity spectrum obtained through Eq. (8) and using the solution of the RDT equations is reported in Fig. 5. The spectra are shown with respect to the wavenumber $\hat{\boldsymbol{\kappa}} = (a/L_1)\boldsymbol{\kappa}$. Differently from the proposed semi-analytical method, solving the RDT equations requires specifying the distance from the stagnation point. The altered turbulence spectra have been hence calculated at a distance from the stagnation point equal to $\xi_1/a = -2.5\times10^{-3}$, while the upwash velocity spectrum representing upstream undistorted conditions have been calculated implementing RDT equations at $\xi_1/a = -20$. The

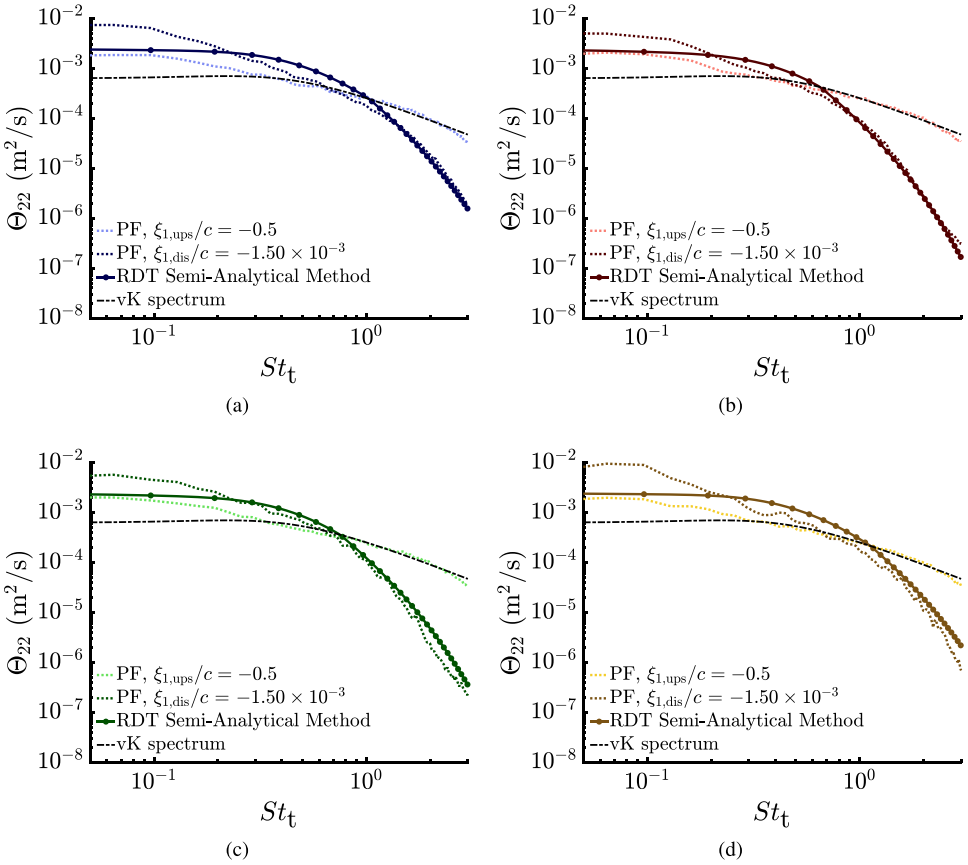

Fig. 4. Comparison between the upwash velocity component spectra obtained with the semi-analytical method based on the RDT findings and the turbulence spectra derived numerically for the (a) NACA 0012, (b) NACA 0012-103, (c) NACA 4412 at $\alpha = \alpha_{ZL}$, and (d) NACA 4412 at $\alpha = 1°$.

von Kármán spectrum has been included as a reference for the undistorted turbulence conditions, together with the two curves representing the two asymptotic trends describing the alteration of the one-dimensional velocity spectrum in the low and the high-wavenumber ranges. The validation has been carried out for a wide range of $L_1/a \gg 1$, reported in the respective plots. For all the cases, the large-scale-turbulence asymptotic trend provides a good approximation of the RDT results up to the non-dimensional wavenumber $\hat{\kappa}_1 = 1$. The high-frequency asymptote overlaps with the spectrum obtained with the solution of the RDT equations for $\hat{\kappa}_1 > \hat{\kappa}_{1,\,CP}$. A good result is also achieved in the transient region, between $1 < \hat{\kappa}_1 < \hat{\kappa}_{1,\,CP}$. This represents a further confirmation that the semi-analytical spectrum provided by Eq. (8) represents a valid methodology to effectively model the alteration of the velocity field due to the interaction of incoming turbulence with a realistic aerofoil geometry across a wide range of conditions.

4.2. Empirical modification of the spanwise coherence length equation

The spanwise coherence length is introduced in Amiet [2] to model the spanwise characteristics of the incoming turbulent flow. This is obtained in Amiet's theory as the ratio between the von Kármán expressions of the two-dimensional wavenumber spectrum $\Psi_{22}(k_1, k_3)$ and the single-wavenumber one $\Theta_{22}(k_1)$ of the upwash velocity component, resulting in

$$l_3(\omega) = \pi \frac{\Psi_{22}(k_1, 0)}{\Theta_{22}(k_1)} = \frac{8L_1}{3}\left[\frac{\Gamma(1/3)}{\Gamma(5/6)}\right]^2 \frac{(k_1/k_e)^2}{\left(3 + 8(k_1/k_e)^2\right)\sqrt{1 + (k_1/k_e)^2}}, \tag{9}$$

with k_e defined as the wavenumber scale of the largest eddies [52] according to

$$k_e = \frac{\pi}{L_1}\frac{\Gamma(5/6)}{\Gamma(1/3)}. \tag{10}$$

Fig. 6 shows the implementation of Eq. (9) together with the spanwise coherence length calculated numerically for the four analysed configurations far upstream at $\xi_{1,ups}/c = -0.5$ and in the stagnation region at $\xi_{1,dis}/c = -1.5 \times 10^{-3}$. A significant discrepancy is found in the low-frequency range with respect to Amiet's analytical expression. Moreover, turbulence distortion appears to alter

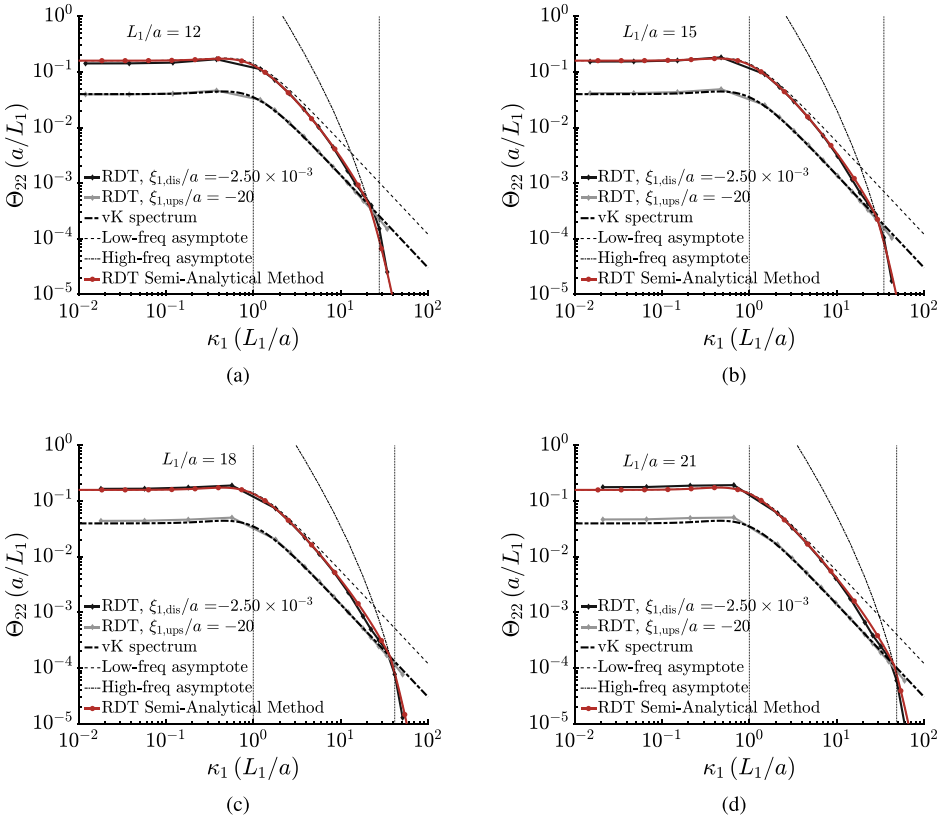

Fig. 5. Comparison between the upwash velocity component spectra obtained with the solution of the RDT equations and the semi-analytical expression of Eq. (8) based on the asymptotic results.

the spanwise coherence as well, inducing an evident increase at low frequencies. This range is associated with the behaviour of large-scale turbulent structures, suggesting that only the distortion of these scales affects the turbulent field in the spanwise direction.

Turbulence-distortion effects in this direction can be investigated by assessing the variation along the stagnation streamline of the correlation length L_{22}^3, relative to the distribution along the direction x_3 of the upwash velocity component u_2 and representative of the energy contained at large turbulence scales. Table 4 reports the value of L_{22}^3 sampled at the upstream position and in the proximity of the stagnation point. This has been calculated using Eq. (A.2). The variation of this parameter, which doubles as the leading edge is approached for all the four configurations taken into account, confirms that the large turbulence scales, as they approach the stagnation region, become increasingly more coherent in the spanwise direction.

This effect can be accounted for by empirically modifying Eq. (9) to include the correlation length of the upwash velocity component L_{22}^3 rather than the streamwise integral length scale L_1. Indeed, it must be noted that the von Kármán expressions for the one and two-dimensional spectra of the upwash velocity component $\Theta_{22}(k_1)$ and $\Psi_{22}(k_1, k_3)$, from which the equation for the spanwise coherence length is obtained, feature the streamwise integral length scale L_1 because they are formulated in the assumption of homogeneous isotropic turbulence. Under this hypothesis, the length scales of the velocity components are related, meaning that the expressions can be modified to make explicit the dependency on the correlation length of the upwash velocity component L_{22}^3. By doing so and by using the local value of L_{22}^3, the effects associated with the alteration of this velocity component can be encompassed. The following expression is hence obtained:

$$l_{3,\mathrm{mod}}(\omega, \xi_1) = \frac{8L_{22}^3(\xi_1)}{3}\left[\frac{\Gamma(1/3)}{\Gamma(5/6)}\right]^2 \frac{(k_1/k_{e,\mathrm{mod}})^2}{\left(3 + 8(k_1/k_{e,\mathrm{mod}})^2\right)\sqrt{1 + (k_1/k_{e,\mathrm{mod}})^2}}, \tag{11}$$

with the wavenumber non-dimensionalised using L_{22}^3 and the parameter k_e, obtained through Eq. (10), modified accordingly through

$$k_{e,\mathrm{mod}}(\xi_1) = \frac{\pi}{L_{22}^3(\xi_1)}\frac{\Gamma(5/6)}{\Gamma(1/3)}, \tag{12}$$

the subscript $_{\mathrm{mod}}$ standing for “modified”.

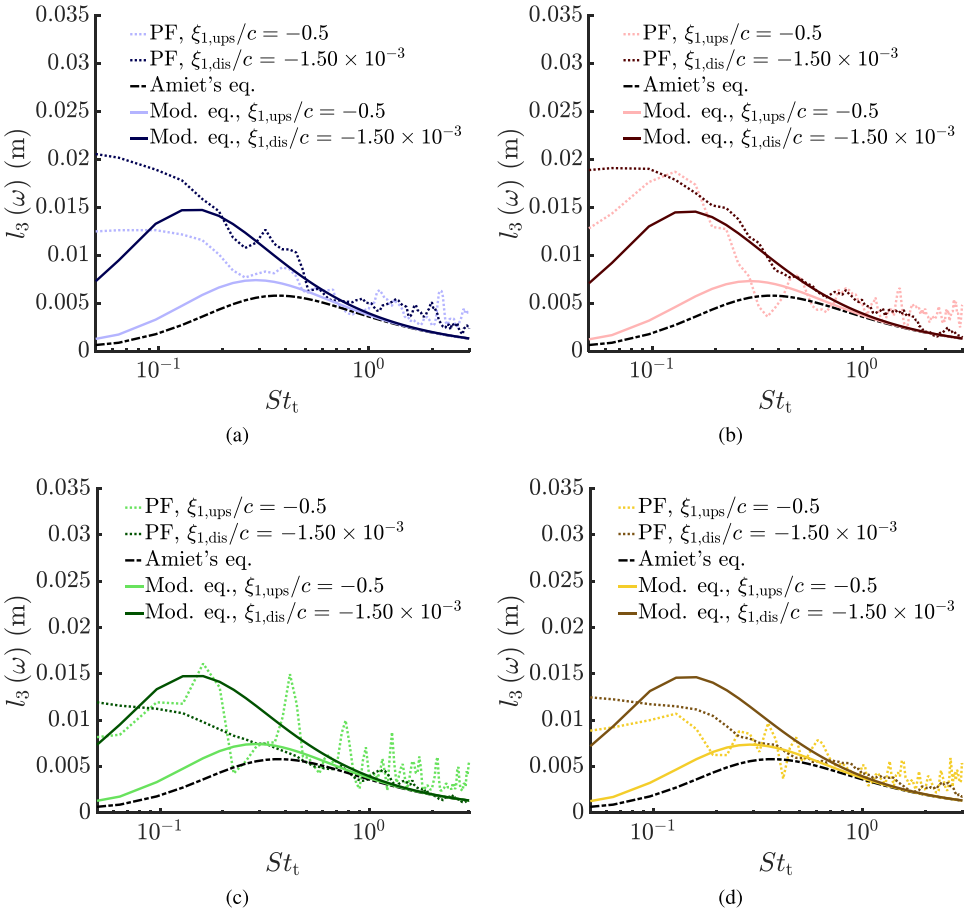

Fig. 6. Spanwise coherence length of the upwash velocity component far upstream ($\xi_{1,\mathrm{ups}}/c = -0.5$) and in the vicinity ($\xi_{1,\mathrm{dis}}/c = -1.5 \times 10^{-3}$) of the stagnation point for the (a) NACA 0012, (b) NACA 0012-103, (c) NACA 4412 at $\alpha = \alpha_{\mathrm{ZL}}$, and (d) NACA 4412 at $\alpha = 1°$. The numerical calculation is shown together with the result of the original analytical expression proposed by Amiet (Eq. (9)) and the proposed semi-empirical approach (indicated as "Mod. eq"., Eq. (11)).

Table 4
Length scale of the upwash velocity component calculated in the spanwise direction in the undistorted ($\xi_{1,\mathrm{ups}}$) and distorted ($\xi_{1,\mathrm{dis}}$) flow-field regions selected to assess turbulence-distortion effects for the four aerofoil configurations.

NACA	$L_{22}^3\big\vert_{\xi_1=\xi_{1,\mathrm{ups}}}$ (m)	$L_{22}^3\big\vert_{\xi_1=\xi_{1,\mathrm{dis}}}$ (m)
0012	7.5×10^{-3}	0.015
0012–103		0.014
4412, $\alpha = \alpha_{\mathrm{zl}}$		0.020
4412, $\alpha = 1°$		0.021

The spanwise coherence length at the stagnation point will be hence retrieved from the local value of the correlation length L_{22}^3, which, following the physical observations for the four aerofoil configurations, can be expressed as twice the value measured far upstream. This allows distortion effects on the spanwise coherence length to be predicted in terms of the upstream undistorted flow conditions.

The implementation of the physics-based correction for the spanwise coherence length (Eq. (11)) is reported in Fig. 6 for the four aerofoil configurations. For the two symmetrical aerofoils, acceptable results are obtained in the modelling of the spanwise coherence length through Eq. (11) for both the undistorted and distorted cases. As in the case of the upwash velocity spectra, the slight turbulence anisotropy is supposed to affect the accuracy of the modelling in the low-frequency range. For the NACA 4412,

instead, a less convincing agreement is obtained to model the altered spanwise coherence length close to the leading edge, meaning that further investigations are still required to propose a more effective and general modification for these configurations.

4.3. Turbulence-distortion effects on the aeroacoustic transfer function

The effects of turbulence distortion on the acoustic response can be demonstrated by focusing on the assumptions underlying the formulation of the transfer function in Amiet's theory and recalling the variation of the velocity field occurring in the stagnation region explained in Section 1 and Section 4.1.

Referring to the overview of the theory in Appendix B, Amiet models the aerofoil acoustic response by calculating the pressure jump on a flat plate using a quasi-steady theory. This approach, which models turbulence-related effects as variations in free-stream velocity and incidence, is valid for large-scale structures interacting with an infinitely thin aerodynamic surface. As a result, surface-pressure distribution and noise scattering are assumed to be generated by large-scale undistorted turbulence. However, the RDT demonstrates that large-scale turbulence is actually distorted because of the presence of the aerofoil, with the resulting alteration of the velocity field consisting of a decrease of the streamwise velocity component fluctuations and an increase of the upwash velocity component fluctuations [20]. This variation can be modelled through asymptotic relations, as explained in Section 4.1. In the limit case $L_1/a \gg 1$, the following expression is obtained for the root-mean-square of the upwash velocity component as a function of the distance from the leading edge along the stagnation streamline

$$\sqrt{\overline{u_2'^2}} = \sqrt{\overline{u_{2,\mathrm{ups}}'^2}} \underbrace{\left[1 + \frac{1}{\left(1 - \frac{x_1}{a}\right)^2}\right]}_{\lambda_2(x_1)}. \tag{13}$$

The detailed procedure to derive this expression is reported in Appendix C. The function $\lambda_2\left(x_1\right)$ has been introduced to describe the variation with respect to upstream conditions. This same distortion mechanism is causing the alteration of the velocity spectra in the low-wavenumber range, detailed in Section 4.1 and modelled through Eq. (2), which indeed features the function $\lambda_2\left(x_1\right)$ squared. Consequently, it has been proven that a higher-energy turbulence input is taken into account once an altered upwash velocity component spectrum is used in Amiet's expression to enhance the modelling of the velocity field in the case of realistic aerofoil geometries. This implies that the transfer function relating the surface-pressure jump to the incoming gust should be scaled accordingly, as explained by Piccolo et al. [26].

This approach marks a significant difference from the procedures currently available in the literature, which model the alteration of the velocity spectrum by imposing the conservation of the variance with respect to upstream conditions [6,22]. Not only is this assumption proven to be physically inaccurate by the results presented herein, but it also produces an incorrect description of the alteration of the velocity field in the low-wavenumber range, associated with the distortion of the large energy-containing eddies. Additionally, it must be kept into account that the unsteady surface loading and, hence, the sound scattering are induced by this higher-energy altered velocity field in the stagnation region [11,15]. Requiring the altered velocity field to be characterised by the same energy content as the upstream undistorted conditions thus results in a poor representation of the noise-generation mechanisms.

A distortion-corrected aeroacoustic transfer function $\mathcal{L}_{\mathrm{dis}}$ can be formulated using the factor $\lambda_2\left(\xi_1\right)$ in the limit $\xi_1 \to 0$ to account for the increase of the gust amplitude with respect to the upstream conditions. The following expression is hence obtained from Eq. (B.5):

$$\begin{aligned}\mathcal{L}_{\mathrm{dis}}\left(x_1, K_1, k_3\right) &= \left(\frac{1}{\lambda_2\left(\xi_1\right)}\right)\Big|_{\xi_1=0} \mathcal{L}\left(x_1, K_1, k_3\right) = \\ &\int_{-L/2}^{L/2} \left(\frac{1}{\lambda_2\left(\xi_1\right)}\right)\Big|_{\xi_1=0} g\left(x_{1,0}, K_1, k_3\right) \mathrm{e}^{-\mathrm{i}\omega x_{1,0}\left(M_\infty - x_1/\sigma\right)/c_\infty \beta^2} \mathrm{d}x_{1,0},\end{aligned} \tag{14}$$

with $\mathbf{x}_0 = \left(x_{1,0}, x_{2,0}, x_{3,0}\right)$ indicating the coordinates of a point on the aerofoil platform area. The reader can refer to Appendix B for the derivation of the expression.

5. Application of the turbulence-distortion modelling methodology to Amiet's model

5.1. Validation with numerical data

The accuracy of the proposed methodology for correcting Amiet's model has been assessed by comparing the prediction with the far-field noise provided by the solid formulation of the FWH analogy in terms of sound pressure level (SPL) and far-field noise directivity patterns. Fig. 7 reports the SPL for an observer at 1.2 m from the leading edge and at an angular position of $\theta = \pi/2$ with respect to the direction of the aerofoil chord. For all aerofoil configurations, the distortion-corrected Amiet's model shows excellent agreement with the noise calculated using the solid formulation of the FWH analogy. The semi-analytical method is able to correctly model the decay of the noise spectrum in the high-frequency range, related to the alteration of the vorticity field characterising the distortion of small-scale structures. An underestimation of less than 5 dB can be observed in the low-frequency range (up to $St_{\mathrm{t}} \simeq 0.2$) for Amiet's model with respect to the FWH results. This is due to the fact that the RDT results, upon which the semi-analytical method

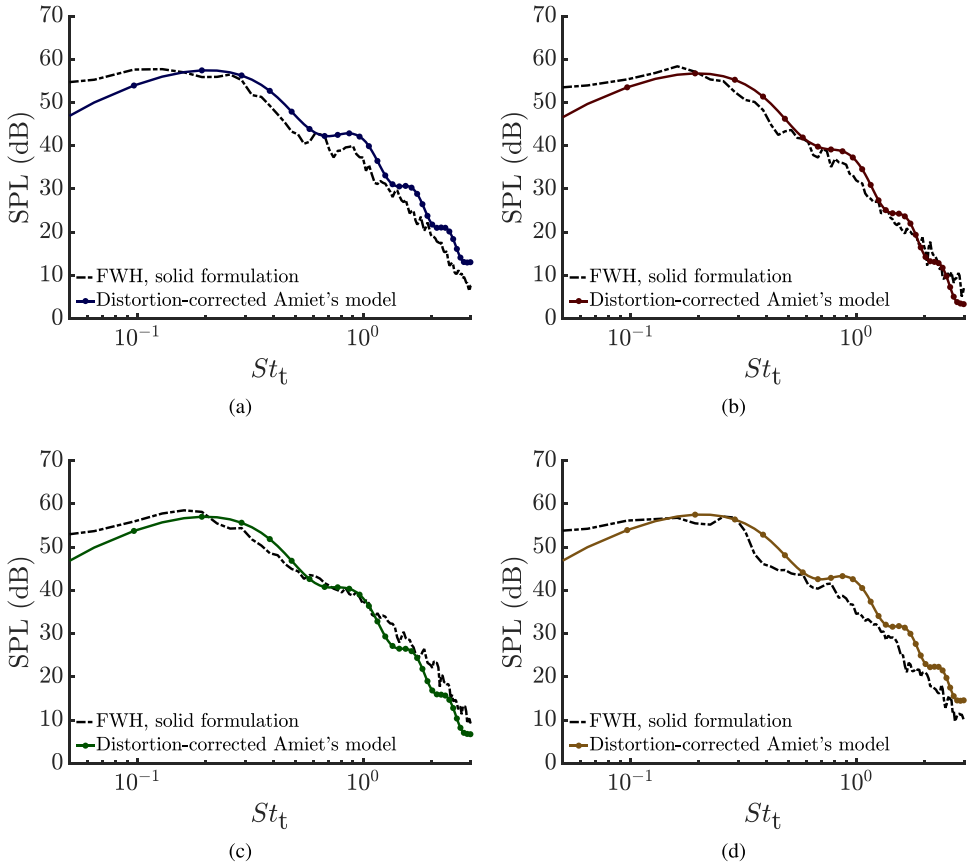

Fig. 7. Sound pressure level calculated with Amiet's model corrected using the turbulence-distortion modelling methodology compared to that calculated with the FWH analogy for the (a) NACA 0012, (b) NACA 0012-103, (c) NACA 4412 at $\alpha = \alpha_{ZL}$, and (d) NACA 4412 at $\alpha = 1°$. The listener position is right above the leading edge ($R = 1.2$ m, $\theta = \pi/2$ with respect to the aerofoil chord direction), while the reference pressure to calculate the SPL is 2×10^{-5} Pa.

is based, are obtained in the assumption of homogeneous and isotropic upstream turbulence and do not take into account the small anisotropy observed for the upwash velocity component spectrum at the exit of the nozzle (see Appendix A). The discrepancy in this frequency range could be reduced by refining the modification of the spanwise coherence length, as it has a slight effect on the noise levels at low frequencies.

The analysis of the far-field noise directivity patterns has been carried out considering the frequency range where leading-edge noise dominates, $St_t = [0.15, 1.5]$. This corresponds to frequencies ranging from 500 Hz to 5 kHz. The comparison between the FWH results and the noise prediction provided by the semi-analytical method is reported in Fig. 8, where the overall sound pressure level (OASPL) is shown. An excellent agreement with FWH can be observed in the four cases at all angular positions, with the exception of a slight overestimation in the angular ranges $-\pi/3 < \theta < 0$ and $0 < \theta < \pi/3$. In this case, the polar coordinates are referred to the direction of the aerofoil chord in order to account for the fact that the cambered aerofoil is at $\alpha \neq 0$.

5.2. Further validation with experimental data

The robustness of the proposed methodology has been further evaluated against experimental data of four symmetrical aerofoils (NACA 0006, NACA 0009, NACA 0012, and NACA 0018) at different free-stream velocities ($U_{\infty,1} = 40\,\mathrm{m\,s^{-1}}$, $U_{\infty,2} = 60\,\mathrm{m\,s^{-1}}$, and $U_{\infty,3} = 80\,\mathrm{m\,s^{-1}}$) investigated by Chaitanya et al. [14]. Data for a flat plate at the same free-stream velocities, also reported by Chaitanya et al. [14], have been used as a reference to compute the relative SPL.

The methodology has been implemented taking as input the turbulence characteristics obtained experimentally ($L_1 = 0.0075$ m, $\mathrm{Tu}_2 = 2.5\,\%$), while the distortion length has been computed using XFOIL. In particular, as proposed in Section 3, the RDT parameter a for the application of the proposed approach has been taken equal to the distance between the peaks of the curvature derivative l_{dis}, which coincides with the distance between the maximum values of the pressure gradient. These values are reported in Table 5 together with the leading-edge radius, provided as a reference. Notably, the latter parameter closely approximates the distortion length, but this relationship holds only for smaller thicknesses and leading-edge radii. As these parameters increase, the distortion

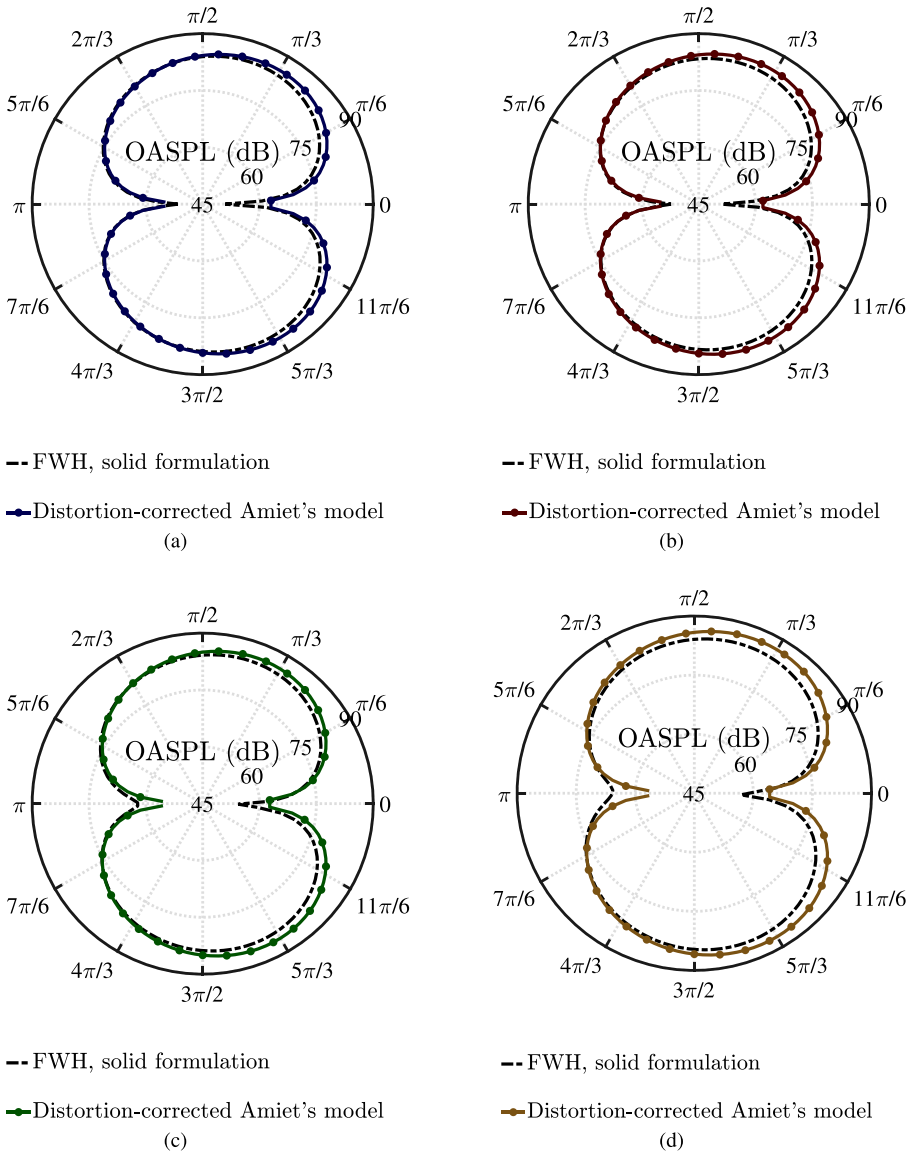

Fig. 8. Far-field noise directivity patterns in the frequency range $St_t = [0.15, 1.5]$ for the (a) NACA 0012, (b) NACA 0012-103, (c) NACA 4412 at $\alpha = \alpha_{ZL}$, and (d) NACA 4412 at $\alpha = 1°$. The corrected Amiet's model implementations are compared with the FWH results. The reference pressure to calculate the OSPL is 2×10^{-5} Pa.

length diverges from the leading-edge radius, as observed in the NACA 0018 and previously in the NACA 0012-103. This indicates that r_{LE} is not the geometrical characteristic directly influencing turbulence distortion.

The comparison between the measured and predicted SPL above the leading edge ($R = 1.2$ m, $\theta = \pi/2$) is shown in Fig. 9, while Fig. 10 reports the relative SPL (ΔSPL) with respect to that radiated by a flat plate. It is important to note that, in the case of the flat plate, the proposed corrected Amiet's model reduces to the canonical formulation. A very good agreement is observed for all aerofoil configurations and free-stream velocities considered, in the frequency range where leading-edge noise dominates ($St_t = [0.15, 1.5]$). For the NACA 0018, for which the application of the methodology is expected to lose validity ($L_1/a \simeq 1$, see Table 5), the agreement is still acceptable – the slope in the frequency range of interest is accurately captured – but not equally satisfactory. However, it is worth noting that the frequency range where leading-edge noise prevails is particularly narrow for this aerofoil due to the early onset of self-noise, as explained by Chaitanya et al. [14]. This characteristic complicates the comparison in this specific case.

This analysis demonstrates that the methodology proposed here is reliable across a wide range of aerofoil thicknesses, leading-edge radii, and free-stream velocities. This also applies in cases where the aerofoil introduces non-negligible disturbances, such as

Table 5
Comparison of the geometrical and mean-flow characteristics obtained using XFOIL for the four NACA aerofoils considered to validate experimentally the semi-analytical method.

NACA	r_{LE} (m)	$\Delta s\left\vert_{\frac{dC_p}{ds}\vert_{\max}}\right.$ (m)	$\Delta s\left\vert_{\frac{dC_p}{ds}\vert_{\max}}\right. = l_{\mathrm{dis}} = a$ (m)	$\frac{L_1}{a}$ [−]
0006	5.95×10^{-4}	6.32×10^{-4}	5.68×10^{-4}	11.87
0009	1.34×10^{-3}	1.19×10^{-3}	1.18×10^{-3}	6.25
0012	2.38×10^{-3}	2.48×10^{-3}	2.48×10^{-3}	3.16
0018	5.36×10^{-3}	5.49×10^{-3}	5.69×10^{-3}	1.37

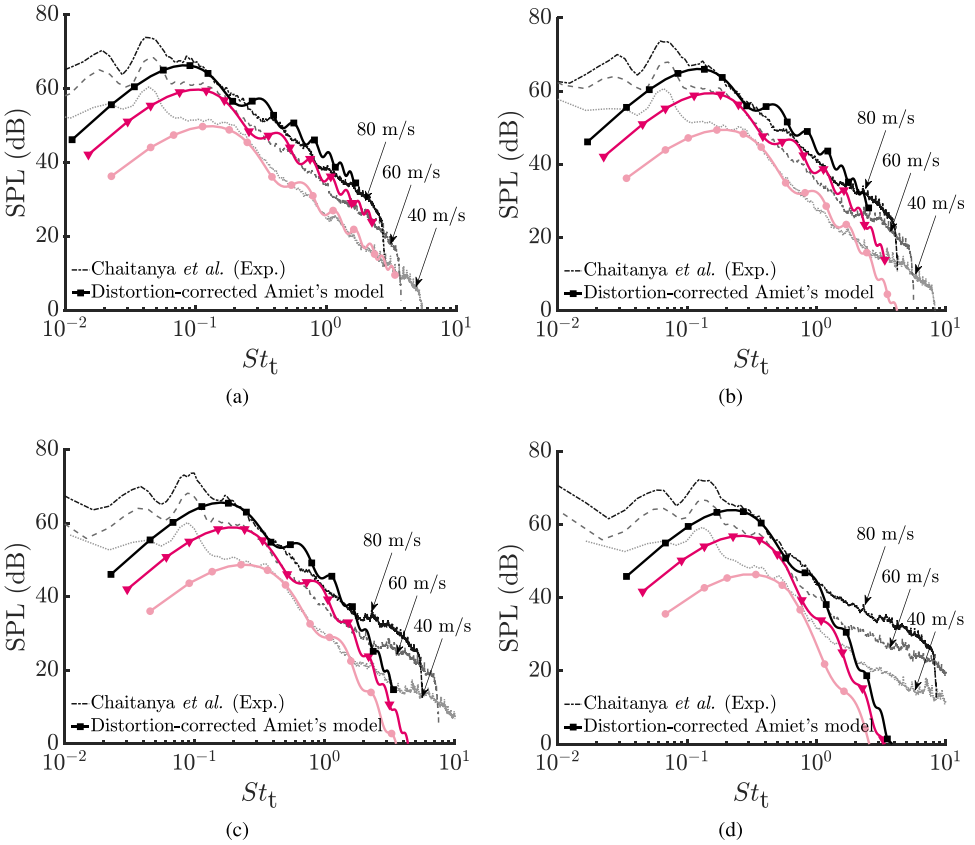

Fig. 9. Sound pressure level calculated with Amiet's model corrected using the turbulence-distortion modelling methodology compared with experimental data from Chaitanya et al. [14] at different free-stream velocities for the (a) NACA 0006, (b) NACA 0009, (c) NACA 0012, and (d) NACA 0018. Amiet's model correction has been implemented using experimental turbulence characteristics and XFOIL data as input. The listener position is right above the leading edge ($R = 1.2\,\mathrm{m}$, $\theta = \pi/2$), while the reference pressure to calculate the SPL is 2×10^{-5} Pa.

those associated with significant thickness or camber. Nevertheless, in these cases, additional analyses are still required to estimate the distortion length, related to the distribution of surface-pressure fluctuations, from geometric and mean-flow properties.

6. Conclusions

The accuracy of Amiet's model for leading-edge noise prediction in the case of realistic aerofoil geometries has been enhanced by accounting for the effects of turbulence distortion on the alteration of the velocity field and on the acoustic response.

These effects have been predicted using RDT asymptotic results, resulting in a methodology that requires as inputs only the turbulence integral length scale and intensity of the upstream undistorted flow and the equivalent RDT characteristic length for aerofoil configurations. This parameter has been taken equal to the space available for the turbulent structures to accelerate and hence deform along the leading edge with the distortion mechanism determined by the size of the eddy with respect to this arc length. This distortion length is identified by the position where the root-mean-square of the pressure fluctuations peak, in turn related to the aerofoil geometry. Although further investigations are necessary to generalise this result to aerofoils of any shape and

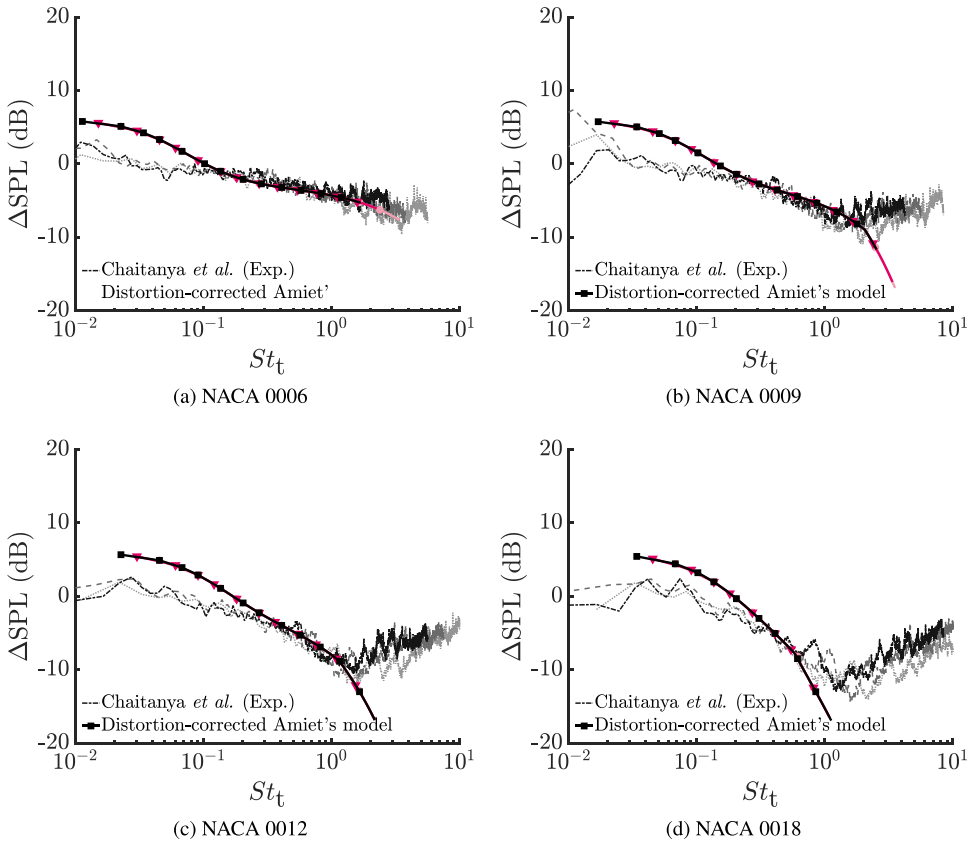

Fig. 10. Difference in sound pressure level between a flat plate and the (a) NACA 0006, (b) NACA 0009, (c) NACA 0012, and (d) NACA 0018, calculated using Amiet's model corrected using the turbulence-distortion modelling methodology and compared with experimental data from Chaitanya et al. [14] at different free-stream velocities (refer to Fig. 9 for legend details). The listener position is right above the leading edge ($R = 1.2\,\mathrm{m}$, $\theta = \pi/2$).

loading conditions, this approach defines a shift in perspective for determining the reference geometric parameter for turbulence distortion. This should be regarded not as a measure of obstacle dimensions – such as the thickness or leading-edge radius proposed so far – but rather as a parameter related to flow acceleration and streamline deflection, in line with the concept of drift used by Lighthill [53], Hunt [20], and Goldstein [54].

The characterisation of the distorted velocity field entails the modelling of the alteration of the frequency spectrum and the spanwise coherence length of the upwash velocity component. The identification of the distortion length has allowed the distorted spectrum of the upwash velocity component to be modelled by interpolating the RDT asymptotic expressions for the alteration of the velocity spectra in the low and the high-wavenumber ranges. This approach has been generalised by comparing these semi-analytical velocity spectra with the solution of the RDT equations in the implementation of Zamponi et al. [51].

The alteration of spanwise coherence length in the distorted region of the flow field, characterised by an increase in the low-frequency range, has been modelled accounting for the variation of the length scale of the upwash velocity component, which doubles with respect to upstream conditions. While this procedure provides an empirical approach to account for this effect, further development is needed to ensure general validity and enhance the modelling in the case of cambered aerofoils.

Regarding the turbulence-distortion effects on the acoustic response, the aeroacoustic transfer function must be corrected to account for the variation of the energy content of the perturbation. This derives from the use as input of a distorted-turbulence term considered at the stagnation point. The required scaling has been implemented using the RDT expression modelling the variation of the variance in the asymptotic case of large-scale turbulence. Remarkably, this result shows that the flat-plate analytical formulation of the aeroacoustic transfer function can be retained for thicker aerofoil geometries once turbulence-distortion effects are taken into account.

This methodology has been validated by applying it to correct Amiet's model for four numerical simulations and four experimental configurations. The numerical simulations involve a NACA 0012, NACA 0012-103, and NACA 4412 at two different loading conditions, while the experimental configurations include a NACA 0006, NACA 0009, NACA 0012, and NACA 0018 at three different free-stream velocities. In the latter case, the distortion length was estimated using XFOIL. An accurate far-field noise prediction was retrieved whenever the methodology was applied within its validity range $L_1/a > 1$, proving the feasibility of this approach to enhance the accuracy of leading-edge noise low-fidelity prediction in the case of realistic aerofoil geometries.

Table A.1
Characteristics of the simulation domain at increasing grid resolutions for the NACA-0012 configuration.

Mesh resolution	Resolution (r_{LE}/finest voxel)	Total amount of voxel (−)
Coarse	6.62	91×10^6
Medium	9.93	287×10^6
Fine	13.25	660×10^6

CRediT authorship contribution statement

Andrea Piccolo: Writing – original draft, Visualization, Validation, Software, Methodology, Investigation, Formal analysis, Conceptualization. **Riccardo Zamponi:** Writing – review & editing, Methodology, Investigation, Formal analysis, Conceptualization. **Francesco Avallone:** Writing – review & editing, Supervision, Software, Funding acquisition. **Daniele Ragni:** Writing – review & editing, Supervision, Funding acquisition.

Declaration of competing interest

The authors report no conflict of interest.

Acknowledgements

The authors thank the European Commission for its financial support through the Horizon 2020 Marie Skłodowska-Curie Innovative Training Network project "zEPHYR" (grant agreement No. 860101). The authors would also like to acknowledge Dr. Stefan Oerlemans and Dr. Steven Buck from Siemens Gamesa Renewable Energy for the fruitful discussions about the topic.

Appendix A. Grid-independence study and validation of the numerical simulations

The grid-independence study and the validation of the present simulations have been discussed in detail by Piccolo et al. [26]. The key points are summarised here.

A.1. Grid-independence study

The independence of the results from the grid discretisation has been evaluated for the baseline case of the NACA 0012. This simulation has been carried out at three increasing grid resolutions, using a refinement factor of 1.5 to pass from the coarse case to the medium one and a refinement factor of 2 to pass from this one to the fine resolution. Information about the three simulations is reported in Table A.1. The analysis has been conducted in terms of sound power level (PWL) and by assessing the time average of the aerodynamic forces integrated on the aerofoil surface.

The PWL has been calculated using the following expression

$$\mathrm{PWL} = \left(\frac{LR}{\rho_\infty c_\infty}\right)\left[\sum_{i=1}^{N-1}\frac{S_{pp}\left(f,\theta_i\right)+S_{pp}\left(f,\theta_{i+1}\right)}{2}\Delta\theta\right], \tag{A.1}$$

employed in the reference experimental campaign of Chaitanya et al. [14] and detailed in Narayanan et al. [55]. In this expression, L indicates the aerofoil span and R is the radius of the array along which the microphones are placed. The PSD $S_{pp}\left(f,\theta_i\right)$ of the far-field noise at the angular position θ_i has been computed using the solid formulation of the FWH analogy. Finally, $\Delta\theta$ indicates the angular separation between two consecutive microphones in the array.

Fig. A.1 reports the PWL obtained in the three different resolution simulations. The sound power level has been shown with respect to the Strouhal number calculated using the aerofoil thickness St_t in the range going from $St_t = 0.15$ to $St_t = 1.5$, where leading-edge noise dominates with respect to other flow-induced noise sources [14]. The frequency ranges where background noise ($St_t < 0.15$) and self-noise ($St_t > 1.5$) prevail in the experimental campaign are shown using dotted lines. The convergence of the simulations is proved by the fact that the three plots coincide in the frequency range of interest for the investigation of leading-edge noise.

The time-averaged aerodynamic forces coefficients, i.e. the lift coefficient $\overline{C}_L$ and the drag-coefficient $\overline{C}_D$, obtained in the three resolution configurations are reported in Fig. A.2 as a function of the total amount of voxels in the respective numerical domains in logarithmic scale. The constant value reached by $\overline{C}_D$ for the medium and the fine configurations confirms that the simulations are converged. Regarding $\overline{C}_L$, the increase in grid resolution does not lead to a constant trend: however, considering the lift curve of a NACA 0012 at the Reynolds number of the present investigation, it can be shown that the variations observed for the time-averaged value of this coefficient correspond to an oscillation of $\simeq 0.25°$ of the angle of attack, which is expected in the case of a turbulent inflow.

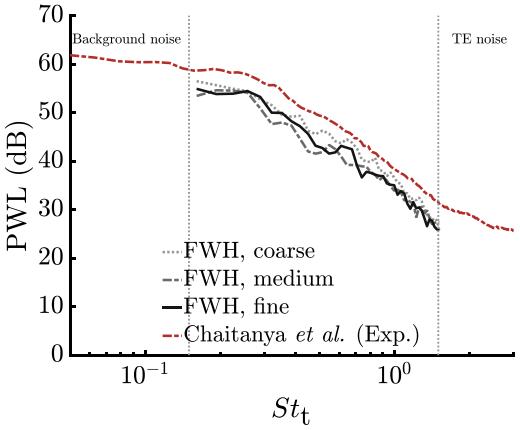

Fig. A.1. Sound power level at three different grid resolutions of the NACA-0012 case for the numerical convergence analysis. The reference power used to calculate the PWL is 10^{-12} W.

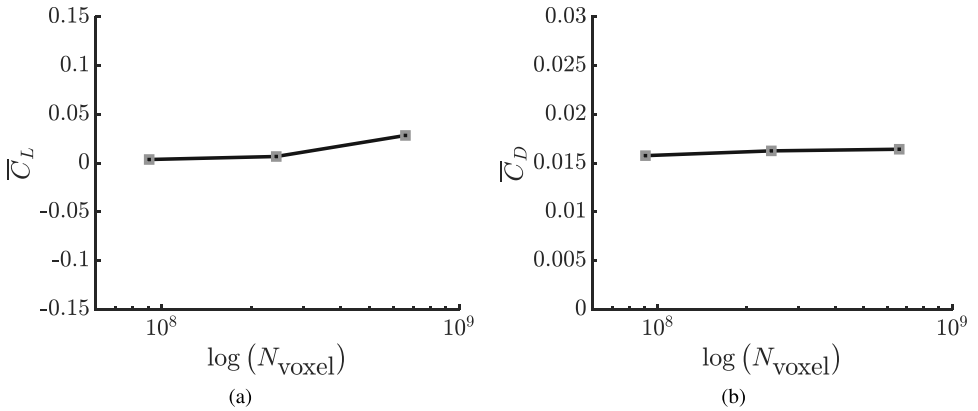

Fig. A.2. Time-averaged trends of the (a) lift coefficient $\overline{C}_L$ and (b) drag coefficient $\overline{C}_D$ at three different grid resolutions of the NACA-0012 case for numerical convergence analysis.

A.2. Aerodynamic and acoustic validations

The aerodynamic validation focuses on the turbulence characterisation, performed in the finest resolution configuration without the aerofoil at the exit of the nozzle. Conversely, the acoustic validation has been carried out using the results of the numerical simulations for the NACA 0012 and the NACA 0012-103, again considered at the finest resolution configuration. The aerodynamic and acoustic numerical acquisitions have been compared to the experimental data from Chaitanya et al. [14], during which the NACA 4412 was not investigated. The aerodynamic validation has been carried out in terms of calculation of time-average, integral length scale, and turbulence intensity of the streamwise velocity component at $x_1/c = -0.033$ upstream of the position of the leading edge. These values have been used in the experimental campaign to scale the von Kármán wavenumber spectrum for the streamwise velocity component, which has therefore been compared with the spectrum sampled numerically at the same position.

As regards the integral length scale, it has been computed using the following expression from Pope [56]

$$L_{ij}^{m}(\mathbf{x}, l) = \int_0^\infty R_{ij}^{m}(\mathbf{m})\,\mathrm{d}l = \int_0^\infty \frac{\overline{u_i'(\mathbf{x}+\mathbf{l}\mathbf{e}_m)\,u_j'(\mathbf{x})}}{u_i'(\mathbf{x})\,u_j'(\mathbf{x})}\mathrm{d}l \quad . \tag{A.2}$$

$R_{ij}^{m}(\mathbf{x})$ indicates the correlation calculated considering a reference location $\mathbf{x}$, with u_i' and u_j' being the turbulent velocity fluctuations components in the ith and jth directions. $\mathbf{e}_m$ is the versor in the mth direction, with the separation distance from the reference location denoted with $l = \mathbf{l}\cdot\mathbf{e}_m$. The time average has been indicated with the operator $\overline{\cdot}$, which can be applied if the assumption of ergodic turbulent fluctuations in the open jet holds.

A value of $59.5\,\mathrm{m\,s^{-1}}$ has been retrieved precisely for the time-average of the streamwise velocity component, which represents the value of the free-stream velocity $\overline{U}_\infty$ (against the $60\,\mathrm{m\,s^{-1}}$ characterising the free stream in the experimental campaign). The turbulence intensity $\mathrm{Tu}_1 = \sqrt{\overline{u_1'^2}}/\overline{U}_\infty$ has been found to be equal to 2.2 %, whereas a value of 2.5 % had been observed in the reference

Table A.2
Comparison of the aerodynamic and turbulence data of the open-jet flow for the numerical simulation and the experimental campaign of Chaitanya et al. [14]. The acquisition has been performed at $x_1/c = -0.033$ with respect to the origin of the reference system.

	$\overline{U}_\infty$ $(\mathrm{m\,s^{-1}})$	Tu_1 (%)	L_1 (m)
Present (LBM-VLES)	59.5	2.2	6.0×10^{-3}
Chaitanya et al. [14] (Exp.)	60	2.5	7.5×10^{-3}

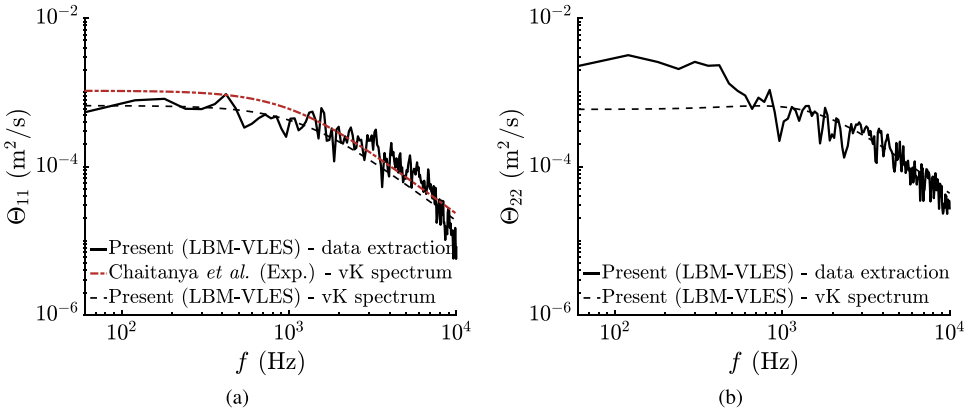

Fig. A.3. Power spectral density of the (a) streamwise velocity component and the (b) upwash velocity component sampled at $x_1/c = -0.033$ with respect to the origin of the reference system. The numerical spectra are compared with the von Kármán (vK) ones scaled using the integral length scale and the turbulence intensity extracted at the same position. For the streamwise-component spectra analysis, also the von Kármán spectrum scaled with the experimental flow conditions of Chaitanya et al. [14] has been included.

experiments. With regards to the streamwise integral length scale L_{11}^3 (abbreviated in L_1), a value of 6.0×10^{-3} m has been achieved in the simulation, with respect to the 7.5×10^{-3} m experimental value. A good agreement is hence obtained between the turbulence characteristics of the reference experimental campaign and those calculated in the present numerical simulation. A summary of these values and their comparison with those obtained in the experimental campaign is provided in Table A.2.

The turbulence spectra for the streamwise velocity component Θ_{11} and upwash velocity component Θ_{22} are illustrated in Fig. A.3. The numerical spectra are shown together with the von Kármán wavenumber ones scaled with the turbulence values from the experiments and the simulation. This is not the case for the upwash velocity spectrum since no related information is reported in the experimental study, nor is the value of the turbulence intensity of this component, which is equal to $\mathrm{Tu}_2 = \sqrt{\overline{u_2'^2}}/\overline{U}_\infty = 2.8$ in the numerical simulations. The following expressions have been employed for the von Kármán spectra

$$\Theta_{11,\mathrm{vK}}(k_1) = \frac{1}{\sqrt{\pi}} \frac{\Gamma(5/6)}{\Gamma(1/3)} \frac{\overline{u_1'^2}}{k_e} \frac{1}{\left[1 + (k_1/k_e)^2\right]^{5/6}}; \tag{A.3}$$

$$\Theta_{22,\mathrm{vK}}(k_1) = \frac{2}{27\sqrt{\pi}} \frac{\Gamma(5/6)}{\Gamma(7/3)} \frac{\overline{u_2'^2}}{k_e} \frac{3 + 8(k_1/k_e)^2}{\left[1 + (k_1/k_e)^2\right]^{\frac{11}{6}}}, \tag{A.4}$$

Note that these are double-sided spectra.

A good match can be observed between the sampled spectrum and the analytical one scaled with the turbulence characteristics obtained numerically in the case of the streamwise velocity component (Fig. A.3(a)). The slight discrepancy with respect to the von Kármán spectrum obtained in the experimental campaign is caused by the difference in the values of the free-stream velocity, integral length scale, and turbulence intensity. Yet, the overall agreement can be considered convincing.

A satisfactory agreement between the sampled spectrum and the von Kármán one scaled with the numerically sampled values is also found for the upwash velocity component (Fig. A.3(b)), although a non-negligible discrepancy can be observed in the low-frequency range, where the analytical expression underestimates the numerical spectrum. This is caused by a slight anisotropy of the flow due to strong section variation downstream of the turbulence-generating grid. The superposition of a rapid distortion on the flow causes indeed an increase of vorticity along the axis of the contraction, which is associated with a decrease in the two normal directions. As a consequence, energy redistributes from the streamwise- towards the upwash- and spanwise velocity fluctuations [57–60], proportionally to the section variation [57], which, in the present case, is particularly high (4.16) with respect

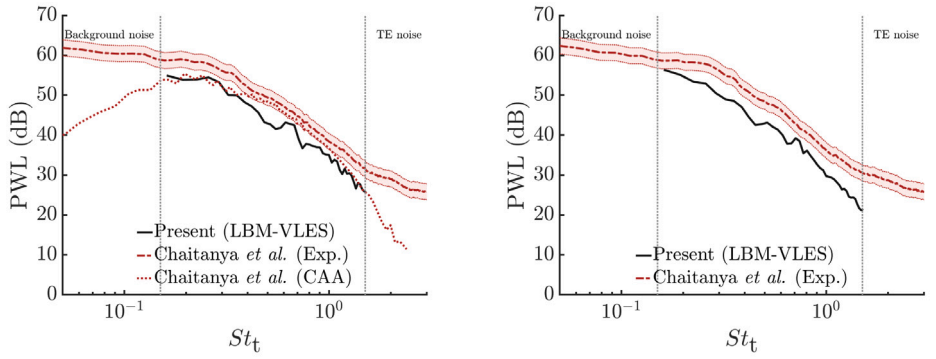

Fig. A.4. Sound power level for the (a) NACA 0012 and (b) NACA 0012-103 configurations with respect to that obtained experimentally by Chaitanya et al. [14]. The reference power used to calculate the PWL is 10^{-12} W.

to those usually employed to decrease flow anisotropy downstream of a grid [58,59,61]. Further details about the turbulence characterisation and the anisotropy are provided by Piccolo et al. [26].

The acoustic data have been validated in terms of PWL. The solid formulation of the FWH analogy has been employed to compute the far-field noise prediction at the microphone locations of the array considered in the experimental campaign, where 18 microphones were placed at angular positions ranging from $\theta = \pi/4$ to $\theta = 3\pi/4$ at a distance $R = 1.2$ m. Fig. A.4 depicts the numerical and experimental PWL, with also the numerical results of Chaitanya et al. [14] reported in the plot for comparison purposes. An agreement within 3 dB has been achieved in the frequency range where leading-edge noise prevails ($St_t \simeq [0.15, 1.5]$) for both NACA 0012 and NACA 0012-103 with respect to the experimental data, which is acceptable considering an estimated measurement uncertainty of ±2 dB [14]. The difference between the numerical and the experimental acoustic data can be traced back to the discrepancy between the turbulence characteristics predicted in the simulation and those obtained experimentally. This also concerns the blockage effect in the wind tunnel caused by the aerofoil, which may differ slightly between the simulation and the experiment.

Appendix B. Amiet's theory for the noise scattered by the leading edge of an aerofoil in a turbulent flow

The low-fidelity noise-prediction method formulated by Amiet [2] is briefly summarised hereafter. Although the notation remains close to the original, the reference system has been modified to be consistent with that of the numerical domain introduced in Section 2.2.

The theory of Amiet is based on two assumptions: the first one requires the incoming turbulence to be *frozen* as it convects and interacts with the aerofoil leading edge. The second one consists of simplifying the aerofoil into an infinitely thin flat plate of chord c and span L, consequently considering negligible the effects of angle of attack and aerofoil geometry on the noise generation and radiation.

Under these two hypotheses, Amiet [2] modelled the incident perturbation interacting with the flat plate at free-stream velocity U_∞ as a two-dimensional upwash velocity gust with amplitude $u_{2,0}$ and wavenumbers k_1 and k_3:

$$u_2\left(x_1, x_3, t\right) = u_{2,0} \mathrm{e}^{\mathrm{i}\left[k_1\left(U_\infty t - x_1\right) - k_3 x_3\right]}. \tag{B.1}$$

The expression of the gust is then used to retrieve the pressure jump across the flat plate by means of the transfer function $g\left(x_1, k_1, k_3\right)$, hence yielding

$$\Delta p\left(x_1, x_3, t\right) = \pi \rho_\infty U_\infty c u_{2,0} g(x_1, k_1, k_3) \mathrm{e}^{\mathrm{i}\left(k_3 x_3 - k_1 U_\infty t\right)}. \tag{B.2}$$

Passing from deterministic to statistical quantities and resorting to the theory of Curle [48], which allows the calculation of the acoustic response of an aerofoil by considering a distribution of dipoles on the surface with the same strength as the loading acting on the surface itself, far-field acoustic pressure S_{pp} at a listener position $\mathbf{x} = \left(x_1, x_2, x_3\right)$ can be retrieved from the cross-spectral density of the pressure jump between the points (x_1, x_3) and (x_1', x_3') on the surface S_{QQ} through the following equation

$$\begin{aligned} S_{pp}(\mathbf{x}, \omega) = & \left(\frac{\omega x_2}{4\pi c_\infty \sigma^2}\right)^2 \iiint S_{QQ}\left(x_1, x_1', \eta, \omega\right) \\ & \times \mathrm{e}^{\frac{\mathrm{i}\omega}{c_\infty}\left[\beta^{-2}\left(x_1 - x_1'\right)\left(M_\infty - \frac{x_1}{\sigma}\right) + \frac{x_3 \eta}{\sigma}\right]} \mathrm{d}x_1 \mathrm{d}x_1' \mathrm{d}x_3 \mathrm{d}x_3'. \end{aligned} \tag{B.3}$$

$\eta = x_3 - x_3'$ is the spanwise separation between the two points considered to calculate the cross-PSD of the surface pressure. The cross-spectral density of the unsteady loading S_{QQ} can then be related to the two-dimensional wavenumber spectrum of the upwash

velocity component of the incoming flow $\Psi_{22}\left(k_1,k_3\right)$ by means of the transfer function $g\left(x_1,k_1,k_3\right)$. Thus, the final expression of Amiet's model to calculate the PSD of far-field noise is

$$S_{pp}\left(\mathbf{x},\omega\right) = \left(\frac{\omega x_2 \rho_\infty c}{2c_\infty \sigma^2}\right)^2 \pi U_\infty \frac{L}{2} \int_{-\infty}^{+\infty} \frac{\sin^2\left[\frac{L}{2}\left(k_3+\frac{\omega x_3}{c_\infty \sigma}\right)\right]}{\left(k_3+\frac{\omega x_3}{c_\infty \sigma}\right)^2 \pi \frac{L}{2}} \times \left|\mathcal{L}\left(\mathbf{x},K_1,k_3\right)\right|^2 \Psi_{22}\left(K_1,k_3\right) \mathrm{d}k_3. \tag{B.4}$$

The assumption of frozen turbulence has been used by considering $K_1 = -\frac{\omega}{U_\infty}$, which shows that a given frequency of the pressure jump is induced by the value $-\omega/U_\infty$ of the streamwise turbulent wavenumber. In the previous expression, $\mathcal{L}$ indicates the total aeroacoustic transfer function, calculated as

$$\mathcal{L}\left(x_1,K_1,k_3\right) = \int_{-L/2}^{L/2} g\left(x_{1,0},K_1,k_3\right) \mathrm{e}^{-\mathrm{i}\omega x_{1,0}\left(M_\infty - x_1/\sigma\right)/c_\infty \beta^2} \mathrm{d}x_{1,0}. \tag{B.5}$$

$\mathcal{L}$ is derived as the sum of two terms, i.e. $\mathcal{L} = \mathcal{L}_1 + \mathcal{L}_2$. These two terms describe the noise emitted by the primary scattering of the incoming turbulence at the leading edge and the back-scattering correction of the incident flow at the trailing edge, respectively [33].

In the case of a large-span aerofoil and considering a listener in the midspan plane of the aerofoil, the following simplified formulation is derived in Amiet [2]

$$S_{pp}\left(x_1,x_2,0,\omega\right) = \left(\frac{\omega x_2 \rho_\infty c M_\infty}{2\sigma^2}\right)^2 \frac{L}{2} \left|\mathcal{L}\left(\mathbf{x},K_1,0\right)\right|^2 \Theta_{22}\left(\omega\right) l_3\left(\omega\right), \tag{B.6}$$

which corresponds to Eq. (1) discussed in the present study. Θ_{22} indicates the PSD of the upwash velocity component, while l_3 represents the spanwise coherence length of the upwash velocity fluctuations (indicated with the superscript $'$), calculated as

$$l_3\left(\omega\right) = \int_0^\infty \sqrt{\gamma^2_{u_2' u_2'}\left(\omega,x_3\right)} \mathrm{d}x_3, \tag{B.7}$$

with γ^2 indicating the magnitude square coherence.

The following expressions have been used for the two terms of the aeroacoustic transfer function $\mathcal{L}_1$ and $\mathcal{L}_2$ [22,62]:

$$\mathcal{L}_1\left(\mathbf{x},k_1,k_3\right) = \frac{1}{\pi}\sqrt{\frac{2}{\left(\frac{k_1 c}{2}+\beta^2\chi\right)\nu_1}} E^*\left(2\nu_1\right) \mathrm{e}^{\mathrm{i}\nu_2}; \tag{B.8}$$

$$\mathcal{L}_2\left(\mathbf{x},k_1,k_3\right) \simeq \frac{\mathrm{e}^{\mathrm{i}\nu_2}}{\pi\nu_1\sqrt{2\pi\left(\frac{k_1 c}{2}+\beta^2\chi\right)}} \left\{\mathrm{i}\left(1-\mathrm{e}^{-2\mathrm{i}\nu_1}\right) + (1-\mathrm{i})\left[E^*\left(4\chi\right) - \sqrt{\frac{2\chi}{\nu_3}}\mathrm{e}^{-2\mathrm{i}\nu_1} E^*\left(2\nu_3\right)\right]\right\}. \tag{B.9}$$

In this expression, $\nu_1 = \chi - \mu x_1/\sigma$, $\nu_2 = \mu\left(M_\infty - x_1/\sigma\right) - \pi/4$, $\nu_3 = \chi + \mu x_1/\sigma$, $\chi^2 = \mu^2 - k_3 c/\left(2\beta^2\right)$, and $\mu = k_1 c M_\infty/\left(2\beta^2\right)$, whereas the function $E^*\left(z\right)$ (with z indicating a generic variable) is expressed as

$$E^*\left(z\right) = \int_0^z \frac{\mathrm{e}^{-\mathrm{i}z'}}{\sqrt{2\pi z'}} \mathrm{d}z' = C_2\left(z\right) - \mathrm{i}S_2\left(z\right), \tag{B.10}$$

C_2 and S_2 being the two Fresnel's integrals:

$$C_2\left(z\right) = \frac{1}{\sqrt{2\pi}} \int_0^z \frac{\cos\left(z'\right)}{\sqrt{z'}} \mathrm{d}z' \tag{B.11}$$

and

$$S_2\left(z\right) = \frac{1}{\sqrt{2\pi}} \int_0^z \frac{\sin\left(z'\right)}{\sqrt{z'}} \mathrm{d}z'. \tag{B.12}$$

Appendix C. Rapid distortion theory: asymptotic analyses in the case of large-scale turbulence

A concise overview of the RDT framework is presented here to introduce the asymptotic analyses. For the basic underlying assumptions and the rigorous analytical formulation, the reader can refer to Hunt [20].

The RDT calculates the alteration of the velocity cross-spectra, auto-spectra and coherence from upstream undistorted flow conditions using the velocity tensor $\mathbf{M}$ to model the distortion of the flow field. In the case of the distorted one-dimensional spectra of the velocity components u_i and u_j $\Theta^*_{ij,\mathrm{dis}}$, generically calculated between the non-dimensional positions $\left(x_1^*,x_2^*\right) = \left(x_1,x_2\right)/a$ and $\left(x_1'^*,x_2'^*\right) = \left(x_1',x_2'\right)/a$ separated by a lateral distance $r_3^* = r_3/a$, the following expression can be obtained as a function of the three-dimensional spectrum $\mathbf{\Phi}^*_{\mathrm{ups}}$ of the upstream turbulence

$$\Theta^*_{ij,\mathrm{dis}}\left(x_1^*,x_2^*;x_1'^*,x_2'^*;r_3^*;\kappa_1\right) =$$

$$\iint_{-\infty}^{\infty} M_{il}\left(x_1^*, x_2^*, \boldsymbol{\kappa}\right)^{\dagger} M_{jm}\left(x_1'^*, x_2'^*, \boldsymbol{\kappa}\right) \boldsymbol{\Phi}_{lm,\mathrm{ups}}^*(\boldsymbol{\kappa})\, \mathrm{e}^{\mathrm{i}\kappa_3 r_3^*} \mathrm{d}\kappa_2 \mathrm{d}\kappa_3. \tag{C.1}$$

The superscript † indicates the complex conjugate, while the non-dimensional wavenumber κ has been introduced in Eq. . The upstream undistorted turbulence spectrum $\boldsymbol{\Phi}_{\mathrm{ups}}^*$ can be modelled using the von Kármán turbulence spectrum [57]

$$\boldsymbol{\Phi}_{ij,\mathrm{ups}}^*(\boldsymbol{\kappa}) = \frac{55 g_1 \left(a/L_1\right)^{2/3} k^2}{36\pi \left[g_2 \left(a/L_1\right)^2 + k^2\right]^{\frac{17}{6}}} \left[\delta_{ij} - \frac{\kappa_i \kappa_j}{k^2}\right], \tag{C.2}$$

where $k^2 = \kappa_1^2 + \kappa_2^2 + \kappa_3^2 = |\boldsymbol{\kappa}|^2$, $g_2 = \pi \Gamma^2(5/6)/\Gamma^2(1/3) = 0.5578$ and $g_1 = g_2^{5/6}/\pi = 0.1957$, with $\Gamma(\cdot)$ being the Gamma function.

The alteration of the velocity field can then be estimated using the canonical turbulence spectrum modelling undistorted turbulence conditions once the velocity tensor has been calculated in the vicinity of the body for each wavenumber component solving four partial differential equations (see Hunt [20] and Zamponi et al. [51]). However, in the asymptotic cases of very large-scale and small-scale turbulence structures interacting with the body, Hunt [20] showed that Eq. (C.1) can be simplified into closed-form expressions. A summarised version of the discussion carried out for large-scale turbulence is reported hereafter to support the derivation of Eqs. (2) and (13). The reader may refer to Sections 5 and 6 in Hunt [20] for the original complete analytical formulation.

C.1. One-dimensional spectra

For large-scale turbulence ($L_1/a \gg 1$), Hunt [20] proved that the spectra can be calculated using the asymptotic expansion of M_{il} valid for $k \to 0$:

$$M_{il} = M_{il}^{(0)} + M_{il}^{(1)} + M_{il}^{(L)} + M_{il}^{(2)} + \cdots, \tag{C.3}$$

with the different terms being of order $\mathcal{O}(1)$, $\mathcal{O}(k)$, $\mathcal{O}\left(k^2 \ln|\kappa_3|\right)$, and $\mathcal{O}\left(k^2\right)$ respectively. This simplification of the velocity tensor indicates that, in the case of a large integral length scale, only the distortion of large turbulent structures can be taken into account to model the alteration of the velocity spectra.

It must be noted that the expansion of M_{il} for $k \to 0$ is valid to $\mathcal{O}\left(k^2 \ln k\right)$, meaning that $M_{il}^{\dagger} M_{jm}$ in Eq. (C.1) can be calculated up to this order and that the integral converges only for $r_3 \neq 0$. However, Hunt [20] showed that by introducing the normalised one-dimensional spectrum

$$\hat{\Theta}_{ij}\left(\hat{\kappa}_1\right) = \left(a/L_x\right) \Theta_{ij}^*\left(\kappa_1\right), \tag{C.4}$$

with $\hat{\kappa}$ introduced in Section 4.1.3, it is possible to express the distorted spectrum using the following expansion as a series in terms of a/L_1

$$\begin{aligned}\hat{\Theta}_{ij,\mathrm{dis}}\left(x_1^*, x_2^*, x_1'^*, x_2'^*, r_3^*, \hat{\kappa}_1\right) = {} & \hat{\Theta}_{ij,\mathrm{dis}}^{(0)}\left(\hat{\kappa}_1\right) + \left(a/L_1\right) \hat{\Theta}_{ij,\mathrm{dis}}^{(1)}\left(\hat{\kappa}_1\right) + \\ & + \left(a/L_1\right)^2 \ln\left(a/L_1\right) \hat{\Theta}_{ij,\mathrm{dis}}^{(L)}\left(\hat{\kappa}_1\right) + \cdots.\end{aligned} \tag{C.5}$$

In this way, the first term of the expansion $\hat{\Theta}^{(0)}$ can be calculated using $M_{il}^{(0)}$, the second term $\hat{\Theta}^{(1)}$ using $M_{il}^{(0)}$ and $M_{il}^{(1)}$, and the third term with $M_{il}^{(0)}$ and $M_{il}^{(L)}$. These terms can be expressed through explicit analytical relations, but a closed-form solution can be identified only for $\hat{\Theta}_{ij}^{(0)}\left(\hat{\kappa}_1\right)$ and $\hat{\Theta}_{ij}^{(1)}\left(\hat{\kappa}_1\right)$.

In the case of the auto spectrum, for which $\mathbf{x}^* = \mathbf{x}'^*$, $i = j$, and $r_3^* = 0$, a further simplification can be applied: $\hat{\Theta}_{ij}^{(1)}$ can be proven indeed to be equal to zero, leading to the following expression for $\hat{\Theta}_{ij}$ as a function of the upstream undistorted spectrum $\hat{\Theta}_{kl,\mathrm{ups}}$

$$\hat{\Theta}_{ij,\mathrm{dis}}\left(\hat{\kappa}_1\right) = F_{ijkl}^{(0)} \delta_{kl} \hat{\Theta}_{kl,\mathrm{ups}}\left(\hat{\kappa}_1\right) + \mathcal{O}(1), \tag{C.6}$$

with δ_{kl} being the Kronecker delta and

$$F_{ij11}^{(0)} = M_{i1}^{(0)}\left(\mathbf{x}^*\right) M_{i1}^{(0)}\left(\mathbf{x}'^*\right), \tag{C.7a}$$

$$F_{ij22}^{(0)} = M_{i2}^{(0)}\left(\mathbf{x}^*\right) M_{i2}^{(0)}\left(\mathbf{x}'^*\right), \tag{C.7b}$$

$$F_{ij33}^{(0)} = M_{i3}^{(0)}\left(\mathbf{x}^*\right) M_{i3}^{(0)}\left(\mathbf{x}'^*\right). \tag{C.7c}$$

The important result is that the PSD of the one-dimensional spectra can be calculated to $\mathcal{O}(1)$, implying that the variation with a/L_1 cannot be obtained [20]. Although this result limits the accuracy of the modelling of the upwash-velocity-spectrum alteration in the low-frequency range using the asymptotic results, it does not affect the noise prediction, as shown in Section 5.

In the case of a cylinder, $M_{il}^{(0)}$ can be expressed by

$$M_{il}^{(0)} = \begin{bmatrix} 1 - \frac{\left(1-\frac{x_1}{a}\right)^2 - \left(\frac{x_2}{a}\right)^2}{\left[\left(1-\frac{x_1}{a}\right)^2 + \left(\frac{x_2}{a}\right)^2\right]^2} & \frac{2\left(1-\frac{x_1}{a}\right)\frac{x_2}{a}}{\left[\left(1-\frac{x_1}{a}\right)^2 + \left(\frac{x_2}{a}\right)^2\right]^2} & 0 \\ -\frac{2\left(1-\frac{x_1}{a}\right)\frac{x_2}{a}}{\left[\left(1-\frac{x_1}{a}\right)^2 + \left(\frac{x_2}{a}\right)^2\right]^2} & 1 + \frac{\left(1-\frac{x_1}{a}\right)^2 - \left(\frac{x_2}{a}\right)^2}{\left[\left(1-\frac{x_1}{a}\right)^2 + \left(\frac{x_2}{a}\right)^2\right]^2} & 0 \\ 0 & 0 & 1 \end{bmatrix}, \tag{C.8}$$

which, substituted in Eq. (C.6) through Eq. (C.7), finally leads to Eq. (2), valid on the stagnation streamline ($x_2/a = 0$). These equations were shown by Zamponi et al. [63] to be valid for modelling the distortion experienced by turbulence interacting with an aerofoil.

C.2. Variance

The cross-variance of the velocity components for lateral separation $r_3^* = 0$ can be calculated to zero order in the asymptotic case $L_1/a \gg 1$ through

$$\overline{u_i'(\mathbf{x}^*)\,u_j'(\mathbf{x}'^*)} = F_{ijll}^{(0)}\left(\mathbf{x}^*, \mathbf{x}'^*\right)\delta_{kl}\overline{u_{k,\mathrm{ups}}' u_{l,\mathrm{ups}}'}. \tag{C.9}$$

This leads then for the variances to

$$\begin{aligned} \overline{u_1'^2(\mathbf{x}^*)} &= \left(M_{11}^{(0)}\right)^2 \overline{u_{1,\mathrm{ups}}'^2} + \left(M_{12}^{(0)}\right)^2 \overline{u_{2,\mathrm{ups}}'^2}, \\ \overline{u_2'^2(\mathbf{x}^*)} &= \left(M_{21}^{(0)}\right)^2 \overline{u_{1,\mathrm{ups}}'^2} + \left(M_{22}^{(0)}\right)^2 \overline{u_{2,\mathrm{ups}}'^2}, \\ \overline{u_3'^2(\mathbf{x}^*)} &= \overline{u_{3,\mathrm{ups}}'^2}. \end{aligned}$$

Expressing the velocity tensor through Eq. (C.8), valid in the case of a cylinder, the following expressions are obtained for the root-mean-square of the velocity components as a function of the distance from the leading edge along the stagnation streamline

$$\sqrt{\overline{u_1'^2}} = \sqrt{\overline{u_{1,\mathrm{ups}}'^2}}\left[1 - \frac{1}{\left(1-\frac{x_1}{a}\right)^2}\right] \tag{C.10a}$$

$$\sqrt{\overline{u_2'^2}} = \sqrt{\overline{u_{2,\mathrm{ups}}'^2}}\left[1 + \frac{1}{\left(1-\frac{x_1}{a}\right)^2}\right] \tag{C.10b}$$

$$\sqrt{\overline{u_3'^2}} = \sqrt{\overline{u_{3,\mathrm{ups}}'^2}}, \tag{C.10c}$$

from which Eq. (13) is obtained.

Data availability

Data will be made available on request.

References

[1] S. Moreau, M. Roger, Competing broadband noise mechanisms in low-speed axial fans, AIAA J. 45 (1) (2007) 48–57, http://dx.doi.org/10.2514/1.14583.

[2] R.K. Amiet, Acoustic radiation from an airfoil in a turbulent stream, J. Sound Vib. 41 (4) (1975) 407–420, http://dx.doi.org/10.1016/S0022-460X(75)80105-2.

[3] R.W. Paterson, R.K. Amiet, Acoustic radiation and surface pressure characteristics of an airfoil due to incident turbulence, in: 3rd Aeroacoustics Conference, American Institute of Aeronautics and Astronautics, Palo Alto, CA, 1976, http://dx.doi.org/10.2514/6.1976-571.

[4] P. Moriarty, G. Guidati, P. Migliore, Recent improvement of a semi-empirical aeroacoustic prediction code for wind turbines, in: 10th AIAA/CEAS Aeroacoustics Conference, American Institute of Aeronautics and Astronautics, Manchester, UK, 2004, http://dx.doi.org/10.2514/6.2004-3041.

[5] S. Moreau, M. Roger, Effect of angle of attack and airfoil shape on turbulence-interaction noise, in: 11th AIAA/CEAS Aeroacoustics Conference, American Institute of Aeronautics and Astronautics, Monterey, CA, 2005, http://dx.doi.org/10.2514/6.2005-2973.

[6] L.D. De Santana, J. Christophe, C. Schram, W. Desmet, A rapid distortion theory modified turbulence spectra for semi-analytical airfoil noise prediction, J. Sound Vib. 383 (2016) 349–363, http://dx.doi.org/10.1016/j.jsv.2016.07.026.

[7] M.E. Goldstein, H. Atassi, A complete second-order theory for the unsteady flow about an airfoil due to a periodic gust, J. Fluid Mech. 74 (4) (1976) 741–765, http://dx.doi.org/10.1017/S0022112076002036.

[8] W. Olsen, J. Wagner, Effect of thickness on airfoil surface noise, AIAA J. 20 (3) (1982) 437–439, http://dx.doi.org/10.2514/3.7922.

[9] H. Atassi, S. Subramaniam, J. Scott, Acoustic radiation from lifting airfoils in compressible subsonic flow, in: 13th Aeroacoustics Conference, American Institute of Aeronautics and Astronautics, Tallahassee, FL, 1990, http://dx.doi.org/10.2514/6.1990-3911.

[10] D.P. Lockard, P.J. Morris, Radiated noise from airfoils in realistic mean flows, AIAA J. 36 (6) (1998) 907–914, http://dx.doi.org/10.2514/2.494.

[11] J.R. Gill, X. Zhang, P. Joseph, Symmetric airfoil geometry effects on leading edge noise, J. Acoust. Soc. Am. 134 (4) (2013) 2669–2680, http://dx.doi.org/10.1121/1.4818769.
[12] S. Oerlemans, Wind Tunnel Aeroacoustic Tests of Six Airfoils for Use on Small Wind Turbines, Technical Report NREL/SR-500-35339, 15007773, National Renewable Energy Laboratory, 2004, http://dx.doi.org/10.2172/15007773.
[13] A. Hall, O. Atassi, J. Gilson, R. Reba, D. Shannon, Effect of leading-edge thickness on high-speed airfoil-turbulence interaction noise, in: 17th AIAA/CEAS Aeroacoustics Conference (32nd AIAA Aeroacoustics Conference), American Institute of Aeronautics and Astronautics, Portland, OR, 2011, http://dx.doi.org/10.2514/6.2011-2861.
[14] P. Chaitanya, J.R. Gill, S. Narayanan, P. Joseph, C. Vanderwel, X. Zhang, B. Ganapathisubramani, Aerofoil geometry effects on turbulence interaction noise, in: 21st AIAA/CEAS Aeroacoustics Conference, in: AIAA Aviation Forum, American Institute of Aeronautics and Astronautics, Dallas, TX, 2015, http://dx.doi.org/10.2514/6.2015-2830.
[15] L. Bowen, A. Celik, M. Azarpeyvand, A thorough experimental investigation on airfoil turbulence interaction noise, Phys. Fluids 35 (3) (2023) 035123, http://dx.doi.org/10.1063/5.0142704.
[16] G. Guidati, R. Bareiss, S. Wagner, R. Parchen, Simulation and measurement of inflow-turbulence noise on airfoils, in: 3rd AIAA/CEAS Aeroacoustics Conference, American Institute of Aeronautics and Astronautics, Atlanta, GA, 1997, http://dx.doi.org/10.2514/6.1997-1698.
[17] J. Gershfeld, Leading edge noise from thick foils in turbulent flows, J. Acoust. Soc. Am. 116 (3) (2004) 1416–1426, http://dx.doi.org/10.1121/1.1780575.
[18] P.D. Lysak, D.E. Capone, M.E. Jonson, Prediction of high frequency gust response with airfoil thickness effects, J. Fluids Struct. 39 (2013) 258–274, http://dx.doi.org/10.1016/j.jfluidstructs.2013.02.006.
[19] D. Kim, G. Lee, C. Cheong, Inflow broadband noise from an isolated symmetric airfoil interacting with incident turbulence, J. Fluids Struct. 55 (2015) 428–450, http://dx.doi.org/10.1016/j.jfluidstructs.2015.03.015.
[20] J.C.R. Hunt, A theory of turbulent flow round two-dimensional bluff bodies, J. Fluid Mech. 61 (4) (1973) 625–706, http://dx.doi.org/10.1017/S0022112073000893.
[21] J.C.R. Hunt, H. Kawai, S.R. Ramsey, G. Pedrizetti, R.J. Perkins, A review of velocity and pressure fluctuations in turbulent flows around bluff bodies, J. Wind. Ind. Aero. 35 (1990) 49–85, http://dx.doi.org/10.1016/0167-6105(90)90210-4.
[22] J. Christophe, application of Hybrid Methods to High Frequency Aeroacoustics (Ph.D. thesis), Université Libre de Bruxelles, 2011.
[23] F.L. dos Santos, L. Botero Bolivar, C. Venner, L. De Santana, Modeling the turbulence spectrum dissipation range for leading-edge noise prediction, AIAA J. (2022) 1–12, http://dx.doi.org/10.2514/1.J061106.
[24] F.L. dos Santos, L. Botero Bolivar, C. Venner, L. De Santana, Inflow turbulence distortion for airfoil leading-edge noise prediction for large turbulence length scales for zero-mean loading, J. Acoust. Soc. Am. 153 (2023) 1811–1822, http://dx.doi.org/10.1121/10.0017458.
[25] A. Piccolo, R. Zamponi, F. Avallone, D. Ragni, Turbulence-distortion analysis for leading-edge noise-prediction enhancement, in: AIAA Aviation 2023 Forum, in: AIAA Aviation Forum, American Institute of Aeronautics and Astronautics, San Diego, CA, 2023, http://dx.doi.org/10.2514/6.2023-3628.
[26] A. Piccolo, R. Zamponi, F. Avallone, D. Ragni, Turbulence distortion and leading-edge noise, Phys. Fluids 36 (12) (2024) 125183, http://dx.doi.org/10.1063/5.0244627.
[27] A. Piccolo, R. Zamponi, F. Avallone, D. Ragni, Towards a novel physics-based correction to Amiet's theory for inflow-turbulence noise prediction, in: 30th AIAA/CEAS Aeroacoustics Conference (2024), American Institute of Aeronautics and Astronautics, Rome, Italy, 2024, http://dx.doi.org/10.2514/6.2024-3121.
[28] P. Mish, W.J. Devenport, An experimental investigation of unsteady surface pressure on an airfoil in turbulence—Part 1: Effects of mean loading, J. Sound Vib. 296 (3) (2006) 417–446, http://dx.doi.org/10.1016/j.jsv.2005.08.008.
[29] P. Mish, W.J. Devenport, An experimental investigation of unsteady surface pressure on an airfoil in turbulence—Part 2: Sources and prediction of mean loading effects, J. Sound Vib. 296 (3) (2006) 447–460, http://dx.doi.org/10.1016/j.jsv.2005.08.009.
[30] F.L. dos Santos, C. Venner, L. Santana, Study of the inflow turbulence distortion for airfoils and cylinders, in: AIAA Aviation 2023 Forum, American Institute of Aeronautics and Astronautics, San Diego, CA, 2023, http://dx.doi.org/10.2514/6.2023-3495.
[31] L.D. De Santana, Semi-Analytical Methodologies for Airfoil Noise Prediction (Ph.D. thesis), KU Leuven, 2015.
[32] R. Miotto, W. Wolf, L. De Santana, Numerical computation of aeroacoustic transfer functions for realistic airfoils, J. Sound Vib. 407 (2017) 253–270, http://dx.doi.org/10.1016/j.jsv.2017.06.037.
[33] M. Roger, S. Moreau, Back-scattering correction and further extensions of Amiet's trailing-edge noise model. Part 1: theory, J. Sound Vib. 286 (3) (2005) 477–506, http://dx.doi.org/10.1016/j.jsv.2004.10.054.
[34] S. Moreau, M. Roger, Back-scattering correction and further extensions of Amiet's trailing-edge noise model. Part II: Application, J. Sound Vib. 323 (1–2) (2009) 397–425, http://dx.doi.org/10.1016/j.jsv.2008.11.051.
[35] S. Succi, The lattice Boltzmann equation: for fluid dynamics and beyond, in: Numerical Mathematics and Scientific Computation, Oxford University Press, Oxford, UK, 2001.
[36] H. Chen, S. Chen, W.H. Matthaeus, Recovery of the Navier-Stokes equations using a lattice-gas Boltzmann method, Phys. Rev. A 45 (8) (1992) R5339–R5342, http://dx.doi.org/10.1103/PhysRevA.45.R5339.
[37] P.L. Bhatnagar, E.P. Gross, M. Krook, A model for collision processes in gases. I. Small amplitude processes in charged and neutral one-component systems, Phys. Rev. 94 (3) (1954) 511–525, http://dx.doi.org/10.1103/PhysRev.94.511.
[38] H. Chen, R. Zhang, P. Gopalakrishnan, Lattice Boltzmann collision operators enforcing isotropy and Galilean invariance, 2017.
[39] H. Chen, R. Zhang, P. Gopalakrishnan, Filtered lattice Boltzmann collision formulation enforcing isotropy and Galilean invariance, 2020, http://dx.doi.org/10.48550/arXiv.2002.02503, arXiv:2002.02503.
[40] M. Chávez-Modena, A. Martínez-Cava, G. Rubio, E. Ferrer, Optimizing free parameters in the D3Q19 multiple-relaxation lattice Boltzmann methods to simulate under-resolved turbulent flows, J. Comput. Phys. 45 (2020) 101170, http://dx.doi.org/10.1016/j.jocs.2020.101170.
[41] W. Li, J. Wang, P. Gopalakrishnan, Y. Li, R. Zhang, H. Chen, Hybrid lattice Boltzmann approach for simulation of high-speed flows, AIAA J. 61 (12) (2023) 5548–5557, http://dx.doi.org/10.2514/1.J063199.
[42] V. Yakhot, S. Orszag, Renormalization group analysis of turbulence. I. Basic theory, J. Sci. Comput. 1 (1) (1986) 3–51, http://dx.doi.org/10.1007/BF01061452.
[43] V. Yakhot, S.A. Orszag, S. Thangam, T.B. Gatski, C.G. Speziale, Development of turbulence models for shear flows by a double expansion technique, Phys. Fluids 4 (7) (1992) 1510–1520, http://dx.doi.org/10.1063/1.858424.
[44] H. Chen, S. Orszag, I. Staroselsky, S. Succi, Expanded analogy between Boltzmann kinetic theory of fluids and turbulence, J. Fluid Mech. 519 (2004) 301–314, http://dx.doi.org/10.1017/S0022112004001211.
[45] B.E. Launder, D.B. Spalding, The numerical computation of turbulent flows, Comp. Meth. App. Mech. Eng. 3 (2) (1974) 269–289, http://dx.doi.org/10.1016/0045-7825(74)90029-2.
[46] F. Farassat, G.P. Succi, A review of propeller discrete frequency noise prediction technology with emphasis on two current methods for time domain calculations, J. Sound Vib. 71 (3) (1980) 399–419, http://dx.doi.org/10.1016/0022-460X(80)90422-8.
[47] D. Casalino, An advanced time approach for acoustic analogy predictions, J. Sound Vib. 261 (4) (2003) 583–612, http://dx.doi.org/10.1016/S0022-460X(02)00986-0.
[48] N. Curle, The influence of solid boundaries upon aerodynamic sound, Proc. R. Soc. 231 (1187) (1955) 505–514, http://dx.doi.org/10.1098/rspa.1955.0191.

[49] P.E. Roach, The generation of nearly isotropic turbulence by means of grids, Int. J. Heat Fluid Flow 8 (2) (1987) 82–92, http://dx.doi.org/10.1016/0142-727X(87)90001-4.
[50] M. Drela, XFOIL: An analysis and design system for low Reynolds number airfoils, in: T.J. Mueller (Ed.), Low Reynolds Number Aerodynamics, Springer, Berlin, Germany, 1989, pp. 1–12, http://dx.doi.org/10.1007/978-3-642-84010-4_1.
[51] R. Zamponi, S. Moreau, C. Schram, Rapid distortion theory of turbulent flow around a porous cylinder, J. Fluid Mech. 915 (2021) A27, http://dx.doi.org/10.1017/jfm.2021.8.
[52] S.A.L. Glegg, W.J. Devenport, Turbulence and stochastic processes, in: S. Glegg, W. Devenport (Eds.), Aeroacoustics of Low Mach Number Flows, Academic Press, 2017, pp. 163–184, http://dx.doi.org/10.1016/B978-0-12-809651-2.00008-4.
[53] M.J. Lighthill, Drift, J. Fluid Mech. 1 (1) (1956) 31–53, http://dx.doi.org/10.1017/S0022112056000032.
[54] M.E. Goldstein, Unsteady vortical and entropic distortions of potential flows round arbitrary obstacles, J. Fluid Mech. 89 (3) (1978) 433–468, http://dx.doi.org/10.1017/S0022112078002682.
[55] S. Narayanan, P. Chaitanya, S. Haeri, P. Joseph, J.W. Kim, C. Polacsek, Airfoil noise reductions through leading edge serrations, Phys. Fluids 27 (2) (2015) 025109, http://dx.doi.org/10.1063/1.4907798.
[56] S. Pope, Turbulent Flows, Cambridge University Press, 2000.
[57] G.K. Batchelor, I. Proudman, The effect of rapid distortion of a fluid in turbulent motion, Quart. J. Mech. Appl. Math. 7 (1) (1954) 83–103, http://dx.doi.org/10.1093/qjmam/7.1.83.
[58] M. Uberoi, Effect of wind-tunnel contraction on free-stream turbulence, J. Aero. Sci. (1956) http://dx.doi.org/10.2514/8.3651.
[59] G. Comte-Bellot, S. Corrsin, The use of a contraction to improve the isotropy of grid-generated turbulence, J. Fluid Mech. 25 (4) (1966) 657–682, http://dx.doi.org/10.1017/S0022112066000338.
[60] R.K. Amiet, J.C. Simonich, R.H. Schlinker, Rotor noise due to atmospheric turbulence ingestion. Part II - Aeroacoustic results, J. Aircr. 27 (1) (1990) 15–22, http://dx.doi.org/10.2514/3.45892.
[61] P. Lavoie, L. Djenidi, R.A. Antonia, Effects of initial conditions in decaying turbulence generated by passive grids, J. Fluid Mech. 585 (2007) 395–420, http://dx.doi.org/10.1017/S0022112007006763.
[62] Y. Rozenberg, Modélisation analytique du bruit aérodynamique à large bande des machines tournantes : utilisation de calculs moyennés de mécanique des fluides (Ph.D. thesis), Ecole Centrale de Lyon, 2007.
[63] R. Zamponi, S. Satcunanathan, S. Moreau, D. Ragni, M. Meinke, W. Schröder, C. Schram, On the role of turbulence distortion on leading-edge noise reduction by means of porosity, J. Sound Vib. 485 (2020) 115561, http://dx.doi.org/10.1016/j.jsv.2020.115561.